REVIEW ARTICLES

Amorphous Iron(III) Oxide—A Review

Libor Machala,[†,‡] Radek Zboril,*[,†,‡] and Aharon Gedanken[§]

Departments of Experimental Physics and Physical Chemistry, Palacky University in Olomouc, Svobody 26, 771 46 Olomouc, Czech Republic, Centre for Nanomaterial Research, Palacky University in Olomouc, Svobody 26, 771 46 Olomouc, Czech Republic, and Department of Chemistry and Kanbar Laboratory for Nanomaterials, Bar-Ilan University Center for Advanced Materials & Nanotechnology, Bar-Ilan University, Ramat-Gan, Israel

Received: August 3, 2006; In Final Form: January 15, 2007

The syntheses of amorphous Fe_2O_3 nanoparticles of varying size and morphology, their magnetic properties, crystallization mechanism, and applications are reviewed herein. The synthetic routes are classified according to the nature of the sample (powders, nanocomposites, films, coated particles). The contributions of various experimental techniques to the characterization of an amorphous Fe_2O_3 phase are considered in this review, including some key experimental markers, allowing its distinction from nanocrystalline "X-ray amorphous" polymorphs (maghemite, hematite). We discuss the thermally induced crystallization mechanisms depending on transformation temperature, atmosphere, and the size of the amorphous particles that predetermine the structure of the primarily formed crystalline polymorph. The controversial description of the magnetic behavior, including an interpretation of the low-temperature and in-field Mössbauer spectra, is analyzed.

1. Amorphous Fe_2O_3 as An Advanced Nanomaterial

In recent years, the iron and iron oxide-based materials, particularly in the form of nanoparticles, have been found to possess unique magnetic, catalytic, optical, sorption, and other properties, enabling their functionalization in many advanced nanotechnological applications. Thus monodispersed iron nanoparticles, fully encapsulated by fullerene-like shells, can serve as a carrier for radioisotopes such as ^{99m}Tc.[1] The incorporation of radioisotopes enables testing and describing the nanometer-scale delivery vehicles for medical diagnostic and therapeutic purposes. The excellent catalytic behavior of iron nanoparticles was utilized for the preparation of pure, aligned, isolated, and dense carbon nanotubes of small diameters and uniform thickness.[2−4] Such carbon nanotubes show unique mechanical, electrical, thermal, magnetic, and capillary properties. These have found application in the field of one-dimensional conductors for the design of nanoelectronic devices, reinforcing fibers in superstrong carbon composite materials, and field emission sources. Magnetic iron oxide nanoparticles (Fe_3O_4, γ-Fe_2O_3) can be widely used as magnetic pigments in recording and information-storage media,[5] catalysis,[6] magnetic fluids,[7] magneto-optical devices,[8] and studies of macroscopic quantum tunneling.[9] It is worthwhile mentioning that nanocrystalline iron oxides have been found to be effective as image-intensifying agents for nuclear magnetic resonance imaging,[10] magneto-caloric refrigeration,[11] medical diagnosis,[12] controlled drug delivery,[13] and magnetic-induced cancer therapy.[14]

However, there are advanced applications where the amorphous nature of an iron oxide phase and a maximum surface area are required, rather than a crystal structure with well-defined properties. Generally, amorphous metal oxides show great industrial potential in solar energy transformation,[15] electronics,[16] electrochemistry,[17] manufacture of magnetic storage media,[18] sorption and purification processes and catalysis.[19,20] In these applications, amorphous iron(III) oxide plays a key role, especially because of its superior catalytic activity, superparamagnetic behavior, and the large specific surface area of the nanoparticles.

In catalysts, amorphous Fe_2O_3 nanoparticles are more active than the nanocrystalline polymorphs or particles of metallic iron of the same diameter thanks to the "dangling bonds" and a higher surface−bulk ratio in the amorphous phase.[20] For example, an amorphous Fe_2O_3 catalyst from sonochemical synthesis was more effective than the nanostructured iron and various crystalline polymorphs for the oxidation of cyclohexane, with a significantly higher selectivity for the target products of cyclohexanol and cyclohexanone.[19,20] This catalytic activity was ascribed to the mesoporous character of the synthesized amorphous Fe_2O_3 sample (see Figure 1). When in the form of a thin layer prepared by the chemical vapor deposition method, amorphous iron(III) oxide can be applied as a photoelectrode and a photocatalyst for splitting water into H_2 and O_2.[21] Amorphous Fe_2O_3 produced by ultrasound radiation was found to be a suitable precursor for the multistep preparation of a magnetic fluid composed of superparamagnetic nanoparticles, which are dispersed in a colloidal solution with hexadecane and stabilized by oleic acid.[22] Among other advanced applications, the nanocomposites of amorphous ferric oxide with SiO_2 are good candidates for use in the field of magneto-optical sensors and magnetic devices due to their attractive properties, including

* To whom correspondence should be addressed. E-mail: zboril@prfnw.upol.cz. Phone: +420585634947. Fax: +420585634954.

† Departments of Experimental Physics and Physical Chemistry, Palacky University.

‡ Centre for Nanomaterial Research, Palacky University.

§ Bar-Ilan University.

10.1021/jp064992s CCC: $37.00
Published on Web 04/03/2007

Dr. Libor Machala received his M.Sc. degree and Ph.D. degree in Experimental Physics at Palacky University in Olomouc (Czech Republic). Since 2002, after finishing his Ph.D., he has been working as a postdoctoral researcher at the Nanomaterial Research Centre at Palacky University in Olomouc. After his short stay at Florida Institute of Technology, he specializes in nanomaterial research, which covers synthesis and characterization of iron-bearing nanoparticles (oxides, ferrates) by thermally induced solid-state reactions. He is well experienced in Mössbauer spectroscopy and thermal analysis techniques. He also gives lectures in atomic and nuclear physics and thermodynamics at Palacky University in Olomouc.

Associate Professor Radek Zboril received his M.Sc. degree and Ph.D. degree in Physical Chemistry at Palacky University in Olomouc (Czech Republic) in 1996 and 2000, respectively. He underwent a series of foreign stays (Wits University, Johannesburg, Republic of South Africa; University of Delaware, U.S.; University of Tokyo, Japan), focused mainly on nanomaterial and nanotechnology research. In 1998, he was awarded for his significant work in the field of thermal decomposition of iron salts by the Ministry of Education of the Czech Republic. His research activities include syntheses, characterization and applications of iron oxide-based nanomaterials, and the study of the mechanism of thermally induced solid-state reactions, mainly using Mössbauer spectroscopy. He is the author or co-author of more than 60 publications and the co-investigator in several international research projects.

soft magnetic behavior, low density, and electric resistivity.[23] In electrochemical applications, amorphous iron(III) oxide used in a lithium intercalation cathode improves its properties, including high electrochemical performance and slow capacity fading.[24] The excellent sorption properties of amorphous Fe_2O_3 thin films doped by Au were employed for the development of

Professor Aharon Gedanken completed his undergraduate studies at Bar-Ilan University (Israel) in 1965 and went on to receive his M.Sc. degree in 1967. He continued his graduate studies at Tel Aviv University under Joshua Jortner and received his Ph.D. in 1973. After a brief postdoctoral period with Otto Schnepp at University of Southern California, Los Angeles, he returned to Bar-Ilan in 1975 as part of the senior faculty where he served as chairman from 1982 to 1985. He has published over 400 scientific papers and worked as a visiting scientist at AT&T Bell Laboratories, National Institute of Diabetes and Digestive and Kidney Diseases and National Institute of Health (Bethesda, MD) between 1989 and 1991. After starting his career as a spectroscopist, in 1993, he switched to nanotechnology research focused on developing methods for the fabrication of novel nanomaterials, mainly using sonochemistry, sonoelectrochemistry, microwave radiation, and reactions under autogenic pressure at elevated temperature.

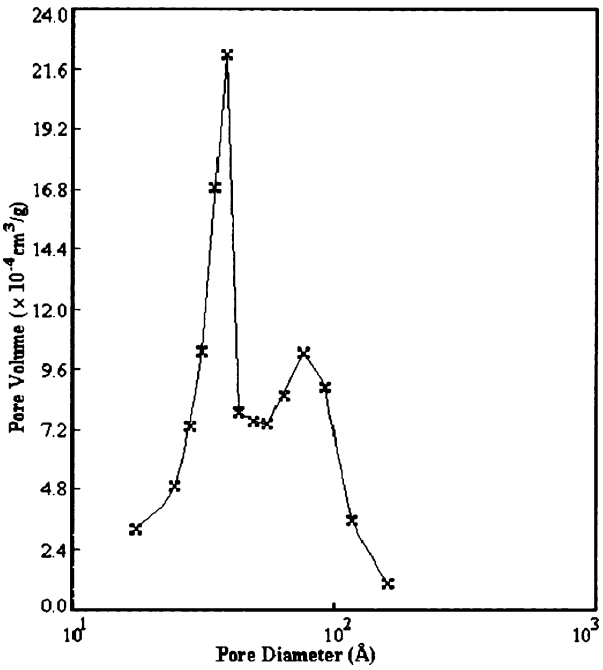

Figure 1. Pore-size distribution for an amorphous Fe_2O_3 mesostructure prepared by a sonochemical method (Srivastava et al.[20]).

humidity sensors with high sensitivity, linearity, and good stability.[25] The linear dependence of the resistance (R) on the relative humidity (RH) is the key sensor parameter, which is determined by the pore-size distribution and specific surface area of the film. Figure 2A demonstrates the variations of the resistance as a function of RH for three iron oxide-based sensors, including (a) ferrihydrite, (b) amorphous Fe_2O_3, and (c) hematite. Clearly, amorphous iron(III) oxide prepared from the ferrihydrite

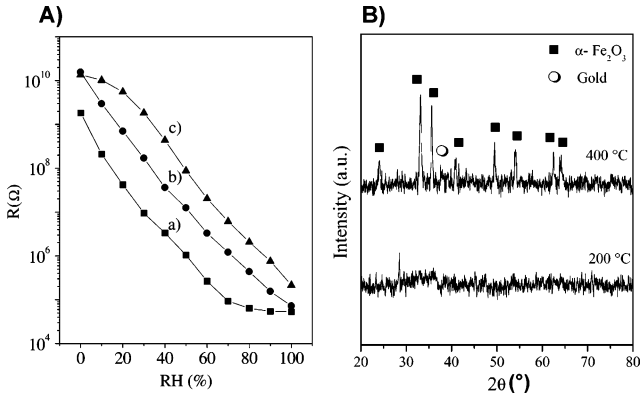

Figure 2. (A) Resistance (R) as a function of relative humidity (RH) for three iron oxide-based sensors: ferrihydrite (a), amorphous Fe_2O_3 (b), and hematite (c). (B) XRD patterns of amorphous Fe_2O_3 and α-Fe_2O_3 thin films prepared by annealing of ferrihydrite at 200 and 400 °C, respectively (Neri et al.[25]).

precursor by heating at 200 °C yields a linear dependence in the whole range of the RH, while the nanocrystalline hematite (α-Fe_2O_3), prepared by heating at 400 °C (see the X-ray diffraction (XRD) patterns in Figure 2B), shows a considerable decrease in the sensitivity at a relative humidity below 30%. This is explained by a decrease in the surface area and by a lowering of the number of active centers for water chemisorption, resulting in a loss of the sensitivity at low RH. The response of the film formed by ferrihydrite ($5Fe_2O_3 \cdot 9H_2O$) is also not linear, showing, however, a saturation effect at high RH > 70%. This occurs when water molecules condense within the pores of the sensor, forming a continuous liquid film. Moreover, such a ferrihydrite sensor reveals a large baseline drift with time, which is attributed to the progressive hydroxylation of the sensing surface layer. This baseline drift is significantly smaller in anhydrous amorphous Fe_2O_3 and can also be reduced by Au doping, which helps to stabilize the amorphous iron oxide phase.

As another advanced application, the modification of the Si surface by amorphous iron(III) oxide is an essential step in the synthesis of magnetic nanocomposites, thus exhibiting several unique properties.[26] The incorporation of sonochemically prepared amorphous iron(III) oxide onto a high-quality Si wafer, followed by annealing the composite, leads to multiple functionality (magnetic, metallic, semiconducting, insulating, and optical) of the material. Upon annealing, Fe(III) is reduced by the silicon to elemental Fe(0) and SiO. The formed SiO is volatile and desorbs immediately. Thus, it is possible to use superparamagnetic amorphous Fe_2O_3 for the preparation of soft, ferromagnetic Fe(0) nanoparticles, uniformly distributed on the flat Si surface (see Figure 3A). This type of material might have a tremendous impact in the area of magnetic semiconductors or spintronics and memory devices. Due to the secondary formation of a β-$FeSi_2$ semiconductor, this composite material exhibits multiple infrared emissions at 1.57, 1.61, and 1.65 μm, which are crucial wavelengths for optical fiber communications (see Figure 3B).

At this point, it is worthwhile stressing that both the above-mentioned and future potential applications of amorphous Fe_2O_3 nanoparticles are strongly related to their intrinsic properties (i.e., size, morphology, surface area, stoichiometry, etc.) and to the nature of the sample. Thus, the characteristics and applicability of amorphous iron(III) oxides differ for pure nanopowders,[27−36] nanocomposites with SiO_2,[37−45] layers and thin films,[46−50] or organically modified coated particles,[51,52] depending on the synthetic route.

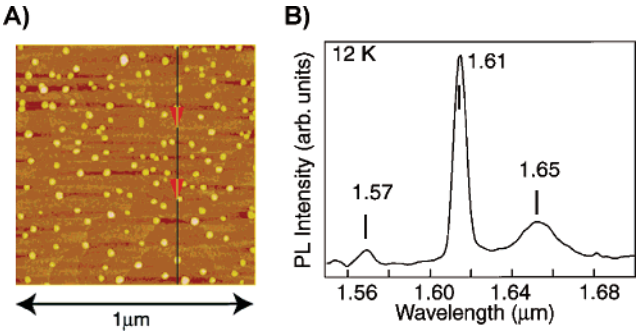

Figure 3. (A) AFM image of the Fe(0) nanoparticles on a Si(111) flat surface prepared by annealing an amorphous Fe_2O_3−Si composite at 850 °C. (B) Photoluminescence spectrum recorded from the Fe−Si composite exhibiting the multiple light emissions related to the formation of a β-$FeSi_2$ semiconductor (Prabhakaran et al.[26]).

This short review follows the previous two reviews on the syntheses and structural and magnetic properties of crystalline α-, β-, γ-, and ϵ-Fe_2O_3 polymorphs,[53] including their characterization by Mössbauer spectroscopy.[53,54] The present work reports on the synthetic routes leading to various forms of amorphous iron(III) oxide, together with their magnetic, size-dependent, and morphological properties. In addition, crystallization mechanisms, techniques suitable for characterization, and "experimental markers" for distinguishing amorphous Fe_2O_3 from nanocrystalline polymorphs are discussed in relation to the authors' experience with Fe_2O_3 nanoparticle systems.[20,22,28−31,52−57]

2. Synthetic Routes toward Amorphous Fe_2O_3 Nanoparticles in Various Forms

A pure ***nanopowder*** without the presence of matrices and other support materials constitutes the most frequent form of amorphous ferric oxide. From the viewpoint of practical applications, it is necessary to prepare such a nanopowder by a cost-effective route, so that one can obtain a sufficient amount of amorphous ferric oxide nanoparticles with a controlled size, narrow size distribution, a certain geometrical shape, and desired properties and functionalities. A few methods for the synthesis of pure amorphous Fe_2O_3 nanopowder have been reported in the literature. Spongelike agglomerates of amorphous Fe_2O_3 particles (3−5 nm) were prepared by the microwave irradiation of an aqueous solution of $FeCl_3 \cdot 6H_2O$ with polyethylene glycol and urea.[27] The larger particles of about 25 nm can be synthesized if pure $Fe(CO)_5$ is irradiated with a high-intensity ultrasonic horn under 1.5 atm of air at 0 °C.[28] The synthesis can be improved and the particle size of amorphous Fe_2O_3 can be controlled by concentration of $Fe(CO)_5$ in decalin during sonication.[29,57] It was found that the lower the concentration of $Fe(CO)_5$ in decalin, the smaller is the particle size of amorphous Fe_2O_3. This sonochemical synthesis allows control not only of the particle size but also of their shape with the help of an applied external homogeneous magnetic field.[30] As a result, highly acicular amorphous particles of 50 nm in length and 5 nm in width were prepared in the presence of an applied field of 0.7 T (Figure 4). The formation of acicular particles was explained by direct magnetic interactions between the particles. In addition to the sonochemical syntheses, iron pentacarbonyl was also found to be a suitable precursor for the preparation of amorphous Fe_2O_3 nanopowder by microwave heating. Thus, the microwave pyrolysis of $Fe(CO)_5$ in refluxing chlorobenzene, which acted as a solvent, resulted in amorphous particles with diameters ranging from 2 to 3 nm.[31] In addition to the syntheses based on ultrasound or microwave irradiation of the suitable

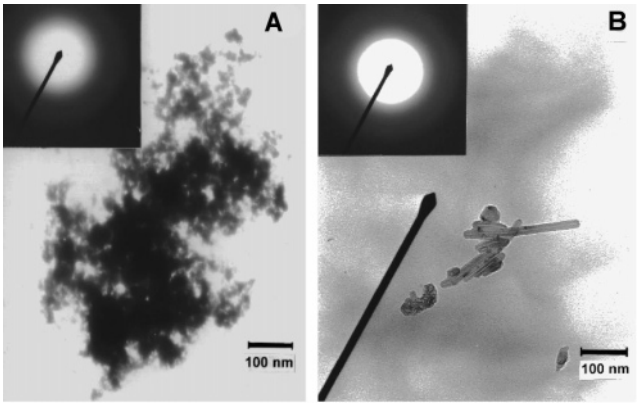

Figure 4. TEM images and selected area electron diffractions of (A) regular amorphous Fe_2O_3 particles prepared by the sonochemical method and (B) acicular amorphous Fe_2O_3 particles prepared by the same route in an applied magnetic field (Prozorov et al.[83]).

liquid Fe precursor, precipitation methods represent another group of preparation routes. Thus, amorphous Fe_2O_3 powders with a specific surface area of about 200 m^2/g were prepared by a homogeneous precipitation of an aqueous solution of $Fe_2(SO_4)_3$ with urea (60−100 °C), followed by the thermal dehydration of precipitates at 200−400 °C.[32] Among the hydrolysis products, ferrihydrite was found to be the most suitable for the preparation of amorphous ferric oxide. Amorphous iron(III) oxide nanopowder with particles of about 3 nm was also precipitated using the principle of reverse micelles. For this purpose, a stock solution of 0.5 M bis(2-ethylhexyl)-sodium sulfosuccinate in hexane was prepared, to which 0.2 M Fe^{3+} and 0.1 M Fe^{2+} water solutions were subsequently added. After that, the obtained solution was slowly mixed with the NH_4-OH solution and some amount of acetone was added. Finally, the ferric oxide precipitate was separated by centrifugation.[33] In a relatively easy way, the short-time hydrolysis (lasting for several seconds) of ferric chloride with a concentration lower than 0.01 mol·dm^{-3} was found to be effective for preparing monodispersed spherical 3−5 nm particles.[35] Another route toward amorphous Fe_2O_3 powder, having an average size of 5 nm, is based on a three-component (a water solution of Fe-$(NO_3)_3$, 2-ethylhexanol, sorbitane mono-oleate) microemulsion technique, followed by heating the precipitates at 250 °C.[34] The particle size can be controlled by the appropriate adjustment of the concentration of ferric salt (i.e., the lower the concentration, the lower is the size). A very specific preparation route, that is, ultrafine powder containing amorphous and nanocrystalline γ-Fe_2O_3 particles, was obtained by a laser-induced vapor-phase reaction with a mixture of $Fe(CO)_5$ and O_2 as reactants and using an IR pulsed CO_2 laser as a light source.[58] The amorphous phase, identified from XRD and X-ray photoelectron spectroscopy (XPS), revealed a particle size range of 5−12 nm in accordance with transmission electron microscopy (TEM) observations. Generally, such a CO_2 laser pyrolysis technique is useful for the synthesis of a variety of nanomaterials, including Fe,[59,60] γ-Fe_2O_3,[61] β-Fe_2O_3,[62] Fe−Si,[63] or Si[64] nanoparticles.

A pure solid-state synthesis of amorphous Fe_2O_3, based on the thermal decomposition of $Fe_4[Fe(CN)_6]_3$ (Prussian Blue) under air, was reported by Zboril et al.[36] The microscopic (atomic force microscopy (AFM), TEM) observations of synthesized Fe_2O_3 nanopowders revealed that the primary ultrasmall particles (1−3 nm) form the spongelike agglomerates (80−150 nm) with a circular cross section and a ratio of lateral-to-vertical dimension near 1 (Figure 5). This method allows controlling the size of the particles through the size of a Prussian

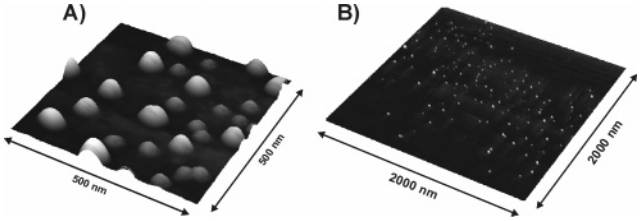

Figure 5. AFM images of amorphous Fe_2O_3 prepared from Prussian Blue: (A) spongelike agglomerates (80−150 nm); (B) dispersed uniformly sized particles (1−3 nm) (Zboril et al.[36]).

Blue precursor, as documented by varying the specific surface area of powders (200−400 m^2/g).

Nanocomposites containing particles dispersed in some matrix represent the most frequent form of the stabilization of an amorphous metal oxide phase. For dispersing such amorphous particles in nonmetallic matrices, sol−gel methods are commonly used.[65−68] The narrow particle size distribution and suppressed interparticle interactions are the main advantages of such nanocomposites in comparison with the powders. All reported sol−gel syntheses of amorphous Fe_2O_3−SiO_2 nanocomposites include the mixing of tetraethoxysilane and ferric salt (nitrate, chloride) alcoholic solutions, followed by the thermal treatment of the gel.[23,38−45] The size of the iron(III) oxide particles can be controlled by both reaction temperature and iron content, an increase which leads to an increase in the particle size and the possible appearance of the crystalline structures (γ-Fe_2O_3 or α-Fe_2O_3).

Layers and thin films of amorphous iron(III) oxide manifest interesting magnetic behavior, different from that of powders and composites. Such layers were developed by the thermal decomposition of an aerosol upon a heated substrate (thin plate of fused quartz). The aerosol was generated by pneumatically or ultrasonically atomizing a solution of $FeCl_3$ (10 wt %) in butylacetate.[46,47] Amorphous Fe_2O_3 films were also produced by a conventional diode sputter deposition method under high sputter gas (Ar) pressure at a substrate temperature of −196 °C.[49] Another deposition route toward amorphous Fe_2O_3 films is based on an electrodeposition process, including a reduction of Fe-$(ClO_4)_3$ or $Fe(ClO_4)_2$ in oxygenated acetonitrile.[48] The experiments were performed at 25 °C under nitrogen in three-electrode cells in a solution of acetonitrile with 0.1 M But_4NClO_4. Furthermore, an amorphous ultrathin film of Fe_2O_3 can be synthesized on partially oriented graphite by the oxidation of an adsorbed monolayer of $Fe(CO)_5$,[50] or on submicrospherical alumina by a sonochemical method.[51]

The coating of particles with a suitable surfactant can modify several properties of amorphous Fe_2O_3 particles, including magnetic behavior, thermal stability, and crystallization temperature. Thus, amorphous Fe_2O_3 particles coated with different alkanethiols were synthesized by the above-mentioned sonication of a $Fe(CO_5)$ solution in decaline with the subsequent exposure of the samples to alkanethiol solutions of different concentrations.[52,69] According to thermogravimetry (TG) and differential scanning calorimetry (DSC) data, the thermal behavior of such powders is strongly dependent on the thiol−Fe_2O_3 molar ratio. If the sonochemical decomposition of Fe-$(CO)_5$ is carried out in the presence of different surfactants, amorphous iron(III) oxide nanoparticles (5−16 nm) coated by undecenoate, dodecyl sulfonate, or octyl phosphonate can be prepared in one step.[70] In this synthetic route, a decane solution of 0.5 M $Fe(CO)_5$ and 0.05 M surfactants was sonicated at 273 K for 3 h under an air atmosphere. The resulting black solution was evacuated to remove any unreacted $Fe(CO)_5$.

The selected syntheses of amorphous Fe_2O_3 particles in different forms and with variable sizes are listed in Table 1, covering preparation conditions and properties of nanoparticles.

3. Magnetic Behavior of Amorphous Fe_2O_3

Over the past years, the increasing interest in nanoparticle systems was related to their specific magnetic behavior, which is markedly different from that exhibited by bulk materials. The size, morphology, local structure of nanoparticles, and enhanced surface effects, together with interparticle interactions, are the key factors influencing the macroscopic magnetic properties of the system such as magnetization, magnetic susceptibility, coercive field, or magnetic transition temperature.[71,72] Such magnetic nanoparticles show remarkable new phenomena such as superparamagnetism, high field irreversibility, high saturation field, or shifted hysteresis loops after field cooling. The majority of authors who studied amorphous iron(III) oxide particles have paid considerable attention to their magnetic behavior. Among experimental techniques, Mössbauer spectroscopy, magnetization and magnetic susceptibility measurements are the most powerful experimental tools suited for this purpose.

3.1. Mössbauer Spectroscopy. Valuable information about the "short-range structure" and magnetic behavior of amorphous iron(III) oxide can be obtained from Mössbauer spectroscopy, mainly when applied at various temperatures and under external magnetic fields. Generally, the room temperature (RT) Mössbauer spectrum of amorphous Fe_2O_3 reveals a broadened doublet. However, the fitting procedures differ among authors. The hyperfine parameters obtained for variously prepared iron(III) oxides are summarized in Table 2. Some authors fit the spectrum by one broadened doublet having, however, non-Lorentzian shape, assuming an electric field gradient distribution as encountered in amorphous materials.[28,29,33,36,45,47,49,73] Other authors[31,38,39,74] fit the RT Mössbauer spectrum of amorphous Fe_2O_3 with two doublets originating from the nonequivalent surface and bulk Fe atoms in amorphous materials (see Table 2). This "surface/bulk" interpretation assumes that the ratio of the spectral lines corresponding to the surface and bulk Fe atoms should strongly relate to the particle size. However, the published data are not quantitatively consistent with this relation (see the values of relative area (RA) in Table 2).

The values of the isomer shift parameter (0.29−0.46 mm/s, relative to metallic iron) obtained at room temperature are typical for high-spin Fe^{3+} ions in octahedral coordination. The high values of the quadrupole splitting parameter reflect a large deviation of the octahedral environment of Fe nuclei from a spherical symmetry. In the group of iron oxides, such a deviation is comparable only with the d-site in the cubic "bixbyite" structure of β-Fe_2O_3. The Mössbauer lines are relatively narrow in comparison with those of nanocrystalline iron(III) oxides,[55,75,76] thus indicating the narrower distribution of electric field gradients than those in nanomaghemite or nanohematite samples. It seems that the origin of the quadrupole splitting distribution in Fe_2O_3 nanoparticle systems can be different in amorphous and in nanocrystalline phases. In the case of amorphous Fe_2O_3 particles, which usually reveal a narrow size distribution, the quadrupole splitting distribution arises rather from the nonequivalent (variously distorted) octahedral environments of Fe nuclei, whereas the broad distributions observed in nanocrystalline iron(III) oxides are frequently related to a broad particle size distribution.

Although the RT Mössbauer spectrum yields important primary information on the structural and magnetic properties of iron(III) oxide nanoparticles, additional data can be obtained from the thermal variation of the Mössbauer spectra (4−300 K). The value of the magnetic ordering temperature, the interval of the coexistence of magnetically nonequivalent components (i.e., the transition range), or the saturation value of the hyperfine magnetic field are strongly affected by the local structure, size, and morphology of particles, and their interactions. Although temperature-dependent Mössbauer spectra were recorded by several authors,[34,36,46,47,49,50,73] their interpretations differ depending on the investigated form of the amorphous iron(III) oxide.

The Mössbauer spectra presented by van Diepen et al. and Heiman et al.[46,47,49] for amorphous Fe_2O_3 *films* show a magnetic ordering temperature of 80 and 100 K, respectively. The magnetic ordering temperature is interpreted as the Néel temperature, below which amorphous Fe_2O_3 is antiferromagnetic. The Mössbauer spectra recorded below the magnetic transition temperature are relatively broad, even at liquid helium temperatures. Such behavior is explained by the random variation of the angles between the local hyperfine field and the axis of the local symmetry over the amorphous iron(III) sample. Thus, the low-temperature spectrum presents a superposition of sextets corresponding to all of these angles. In comparison with the values published for nanocrystalline γ- and α-Fe_2O_3 (>50 T), the reduced value of the magnetic hyperfine field of amorphous Fe_2O_3 at 5 K (47 T) is presented as an identification sign of the amorphous nature of the sample.

The thermal evolution of the shape of the Mössbauer spectrum of amorphous Fe_2O_3 *nanopowders*, synthesized from Prussian Blue (Figure 6), was explained by the strong interaction between superparamagnetic particles with a significant shift of the magnetic regime from inhomogeneous blocking to the glass collective state, as in spin glass.[36,77] The fast temperature variation of the spectral area of superparamagnetic fraction indicates that the transition to superparamagnetism retains the memory of the collective state. The observed independence of the blocking temperature on the size of amorphous Fe_2O_3 prepared from Prussian Blue confirms the suggested model. Below the blocking temperature, a fast increase in the hyperfine field was observed with decreasing temperature. Nevertheless, its saturation value measured at 4 K remains reduced ($\approx$49 T). It seems that the reduced hyperfine field at low temperature is one of the key markers of the amorphous nature of iron(III) oxide nanoparticles, independently of their synthesis and form (powder, film). It is important to note that the average quadrupole shift parameter is near zero due to a random distribution of angles between the magnetic hyperfine field and the electric field gradient in the amorphous Fe_2O_3 phase.

The in-field Mössbauer spectra were measured for amorphous Fe_2O_3 in the form of pure nanopowder,[73] and also for the nanoparticles hosted in a silica aerogel matrix,[78] both in an external field applied parallel to the γ-ray direction. Independently of the different degrees of interparticle interaction, the spectra display negligible changes in comparison with those recorded in a zero-applied field at the same temperature. In particular, the intensities of lines 2 and 5 remain almost unchanged. This fact supports the very specific magnetism of amorphous Fe_2O_3, as the intensities of these lines are reduced or enhanced for ferromagnetic (ferrimagnetic) and antiferromagnetic materials, respectively, if an external field is applied parallel to the γ-ray direction. This unusual response to the applied field in a Mössbauer spectrum represents one of the principal markers for how to identify an amorphous Fe_2O_3 phase and distinguish it from nanocrystalline polymorphs (see section 5). In the case of a nanopowdered sample with a high degree of interparticle interaction, the unchanged line intensities in the

TABLE 1: Survey of the Selected Syntheses of Amorphous Fe_2O_3[a]

synthetic route	precursors	exptl condns	condns allowing the control of the particle size or morphology	sample nature	particle size (nm)	note	ref
microwave irradiation	aqueous soln of $FeCl_3 \cdot 6H_2O$, polyethylene glycol, and urea	650 W microwave oven		P	3−5	agglomerates of fine particles	27
sonochemical synthesis	pure $Fe(CO)_5$	1.5 atm of air at 0 °C		P	25	$S = 79$ m^2/g	28
sonochemical synthesis	$Fe(CO)_5$, decalin	1.5 atm of air at 0 °C	4 M soln of $Fe(CO)_5$ in decalin	P	18.7	$S = 148$ m^2/g	29
			1 M soln of $Fe(CO)_5$ in decalin	P	14.7	$S = 181$ m^2/g	29
			0.25 M soln of $Fe(CO)_5$ in decalin	P	14.2	$S = 207$ m^2/g	29
			1 M soln of $Fe(CO)_5$ in decalin, external magnetic field of 0.7 T	P	5 × 50	acicular particles	30
microwave pyrolysis	$Fe(CO)_5$, chlorobenzene	air		P	2−3	agglomerates (25−40 nm) of fine particles	31
precipitation	aqueous soln of $Fe_2(SO_4)_3$, urea	60−100 °C		P		$S = 200$ m^2/g	32
precipitation	aqueous solns of Fe^{3+} and Fe^{2+}	aqueous solns of AOT and NH_4OH used as micellar solns		P	3	acetone used as a precipitation agent	33
microemulsion technique followed by precipitation and heating of precipitate	aqueous soln of $Fe(NO_3)_3$, 2-ethylhexanol, and sorbitane mono-oleate	heating temp of 250 °C, $Fe(NO_3)_3$ concn of 0.312%		P	5	NH_4OH used as a precipitation agent	34
hydrolysis followed by thermal dehydration	aqueous soln of $FeCl_3$ and HCl	$FeCl_3$ concn of 0.01 mol·dm^3		P	3−5	spherical particles	35
thermally induced solid-state decompn	$Fe_4[Fe(CN)_6]_3$	air, decompn temp of 250 °C	precursor particle size: 18−29 nm	P	1−3	$S = 400$ m^2/g	36
			precursor particle size: 56−66 nm	P	2−4	$S = 200$ m^2/g	
sol−gel followed by thermal treatment	alcoholic soln of $Si(OC_2H_5)_4$ and aqueous soln of $Fe(NO_3) \cdot 9H_2O$	Fe−Si ratio = 0.4, gel heated at 300 °C	temp, iron content in nano-composite	N	2	$S = 212$ m^2/g	23, 38−45
thermal decompn of aerosol	$FeCl_3$ soln in butylacetate	decompn temp of 250 °C		F		aerosol generated pneumatically or ultrasonically	46, 47
diode sputter deposition	Fe_2O_3 target	−196 °C, high sputter gas (Ar) pressure		F		alternatively Fe_3O_4 target and O_2 plasma can be used	49
electrodeposition process (oxidation of electrodeposited metal by dissolved oxygen)	$Fe(ClO_4)_3$, $Fe(ClO_4)_2$, and acetonitrile	25 °C, under nitrogen in three-electrode cells in soln of acetonitrile with 0.1 M But_4NClO_4		F		platinum counter electrode Ag/Ag^+ reference electrode	48
surface oxidation of precursor monolayer	$Fe(CO)_5$	graphite surface used as a support material, 1000 °C, 10^{-5} Torr		F		precursor monolayer adsorbed from the gas state	50

[a] P, powder; N, nanocomposite; F, thin film or layer; *S*, surface area.

TABLE 2: Hyperfine Parameters of RT Mössbauer Spectra of Amorphous Iron(III) Oxides Prepared by Different Routes[a]

component	δ_{Fe} (mm/s)	ΔE_Q (mm/s)	$\Gamma_{1/2}$ (mm/s)	RA (%)	size (nm)	sample nature	ref
D	0.34	1.01	0.62	100		F	47
D	0.33	1.13	0.68	100		F	49
D	0.34	0.87	0.56	100	4−6	N	45
D	0.42	0.93	0.70	100	25	P	28, 29
D	0.33	0.84	0.52	100	1−4	P	36
D	0.39	0.68		100	3	P	33
D	0.36	1.07	0.52	75	5	P	34
S	0.12−0.16		0.50−0.65	25			
DI	0.29	0.61	0.36	42	3−4	N	39
DII	0.28	1.07	0.48	58			
DI	0.34	0.66	0.38	44	2	N	38
DII	0.34	1.13	0.51	56			
DI	0.38	0.56	0.30	66	2−3	P	31
DII	0.40	0.96	0.30	34			
DI	0.46	0.69	0.44	20	3	P	74
DII	0.46	1.19	0.44	80			

[a] δ_{Fe}, isomer shift relative to metallic iron; ΔE_Q, quadrupole splitting; $\Gamma_{1/2}$, full width at half-maximum; RA, relative area; D, doublet; S, singlet; P, powder; N, nanocomposite; F, thin film or layer.

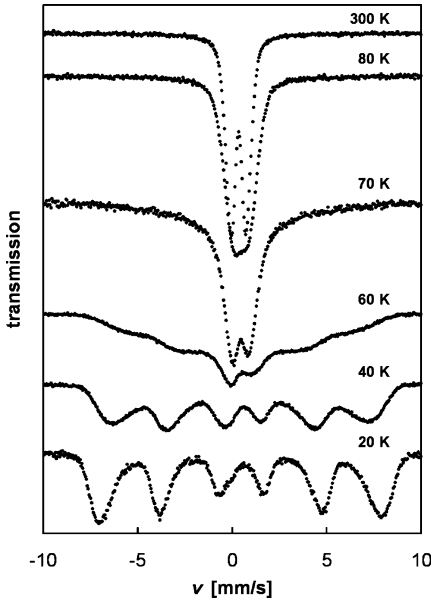

Figure 6. Temperature-dependent Mössbauer spectra (20−300 K) of the amorphous Fe_2O_3 nanopowder prepared from Prussian Blue (Zboril et al.[36]).

zero-field and in-field spectra can be interpreted through a spin-glass-like behavior.[36,73] For the isolated non-interacting amorphous Fe_2O_3 particles, the speromagnetic model is assumed to explain the same profiles of Mössbauer spectra recorded without and in the large external magnetic field.[78]

A speromagnetic model was originally developed for a description of the magnetic behavior of ultrasmall amorphous particles below ordering temperature, where in-field Mössbauer spectroscopy is used as the key experimental support. Generally, speromagnetism is a variety of magnetic order in amorphous or disordered materials where the atomic spins are frozen in essentially random orientations with an isotropic probability distribution. In speromagnetic materials, the magnetism mainly depends on the balance between exchange interactions and magnetic anisotropy. Such phases exhibit the absence of long-range magnetic ordering below a magnetic transition temperature despite the presence of strong antiferromagnetic exchange interactions. The speromagnetic structure differs from the paramagnetic one in the sense that magnetic moments do not fluctuate in time. Contrary to the spin-glass systems, where the random spin structure occurs at the level of domains, the speromagnetic phase is characterized by the spin disorder in the atomic-nearest-neighbor scale with the adjacent spins being uncorrelated in the orientation. The application of an external field does not induce any long-range ordering in the speromagnetic structure due to the absence of the principal crystallographic axis in an amorphous particle. As a result, the random spin arrangement is preserved even in high external fields, which is reflected by nearly the same profile of zero-field and in-field Mössbauer spectra.[79−82]

3.2. Magnetic Susceptibility and Magnetization Measurements. Similar to Mössbauer spectra, the magnetic susceptibility and magnetization curves of amorphous Fe_2O_3 are significantly affected by the synthetic route determining the particle size distribution and the degree of interparticle interaction. The curve of alternating current (ac) susceptibility versus temperature for amorphous Fe_2O_3 nanopowder, prepared from Prussian Blue,[36] displays a maximum corresponding to a magnetic transition temperature at about 50 K. The shape of the χ-vs-T curve can provide information on the distribution of the energy barriers (E_B). For an inhomogenous blocking process, the peak width increases if the E_B distribution broadens. The interactions narrow the E_B distribution, and as a result, a relatively narrow peak is observed in the sample of amorphous Fe_2O_3 nanopowder, representing a strongly interacting system.[77] These conclusions are in good agreement with the Mössbauer measurements.

Above a magnetic ordering temperature, the temperature dependence of reciprocal susceptibility ($1/\chi$ vs T) fulfills the Curie−Weiss law, reflecting the paramagnetic or superparamagnetic behavior of amorphous Fe_2O_3.[39,46,47,49] The values of the effective magnetic moments per iron atom calculated from the linear slope of the $1/\chi$-vs-T curve above the magnetic ordering temperature were found to be very low: $2.5\mu_B$ for the layers prepared by decomposing an aerosol from an $FeCl_3$ solution in butylacetate,[46,47] $2.8\mu_B$ for the nanocomposite from sol−gel synthesis,[39] and $3.0\mu_B$ for the film obtained by the sputter deposition process.[49] Independently on the synthetic routes, these values are much lower than the value expected for Fe^{3+} ions ($\sim 5\mu_B$). It seems that such a decrease in the effective magnetic moment per one iron atom is not accidental; however, its explanation is rather questionable. The reduced value of effective magnetic moment was usually ascribed to the formation of magnetic clusters[46,47,49] and to an extremely low particle size with a high contribution of the surface anisotropy.[36] Indeed, we cannot exclude that this phenomenon can be directly related to the essence of magnetism of amorphous Fe_2O_3 (speromagnetism, spin-glass-like behavior). Nevertheless, this issue needs further experimental and theoretical clarification.

As the most powerful measuring tools, sensitive to the influence of the particle size, morphology, and interparticle interactions on the magnetic properties of amorphous Fe_2O_3, the zero-field-cooled (ZFC) and field-cooled (FC) magnetization measurements are frequently applied. The differences in the magnetic characteristics of interacting and non-interacting particles of amorphous Fe_2O_3 are clearly seen in Figure 7. For a nanopowdered sample, representing a strongly interacting system, the ZFC curve shows a broad maximum at T_{max} corresponding to the average blocking temperature through the sample.[83] The FC curve departs from the ZFC curve at the magnetic irreversibility temperature (T_{irr}), corresponding to the blocking temperature of the largest particle. The FC curve

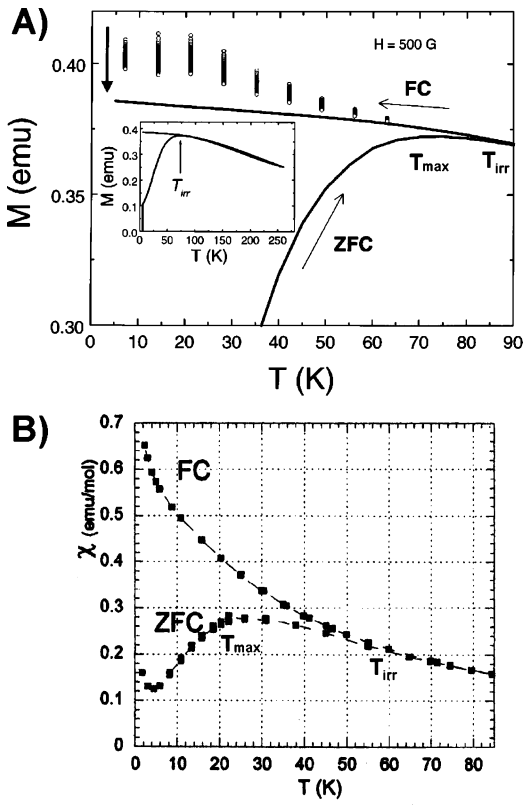

Figure 7. FC−ZFC magnetization curves for (A) amorphous Fe_2O_3 nanopowder [the vertical lines depict the relaxation measurements at different temperatures (Prozorov et al.[83])] and (B) $Fe_2O_3-SiO_2$ nanocomposite (Cannas et al.[45]).

recorded for amorphous Fe_2O_3 nanopowder (see Figure 7A) remains practically constant below T_{irr},[33,83] which is typical for strongly interacting nanoparticle systems including γ-Fe_2O_3[84,85] and α-Fe_2O_3 nanopowders.[86] The shape of the ZFC−FC curves in such systems with strong interparticle interactions was explained by a progressive blocking of the magnetic moments of the superparamagnetic particles, with a distribution of relaxation times. The interpretation based on strong interparticle interactions was also supported by magnetic relaxation measurements showing logarithmic decay of relaxation time with temperature, as depicted by vertical lines in Figure 7A. The interactions also modify the anisotropy energy barrier (E_B), leading to an increase of T_{max} and a narrowing of the E_B distribution.[43,84,86−89] The maximum of the FC curve, followed by a plateau at lower temperatures, is similar to the behavior observed in spin glass, characterized by a random cooperative freezing of spins or spin clusters at a well-defined transition temperature.[33,86,90] For comparison, Figure 7B shows the ZFC−FC curves measured for amorphous Fe_2O_3 dispersed in a SiO_2 matrix, a nanoparticle system without interparticle interactions.[39,45] Below T_{irr}, the FC curve ascends steeply with a decreasing temperature and T_{max} is shifted to a much lower value than in the case of amorphous Fe_2O_3 nanopowder.[39]

In addition to the degree of interparticle interactions, the FC−ZFC curves are strongly affected by the particle size distribution and particle morphology.[30,91] With an increasing particle size, T_{max} shifts to the higher temperatures due to the increase in the average blocking temperature. As the particle size distribution broadens, the values of T_{max} and T_{irr} differ more notably and a broadening of the ZFC curve is observed.[84] The role of the particle morphology has been studied by Prozorov et al. for globular particles synthesized by the sonochemical irradiation of $Fe(CO)_5$ and for acicular particles prepared by the same route

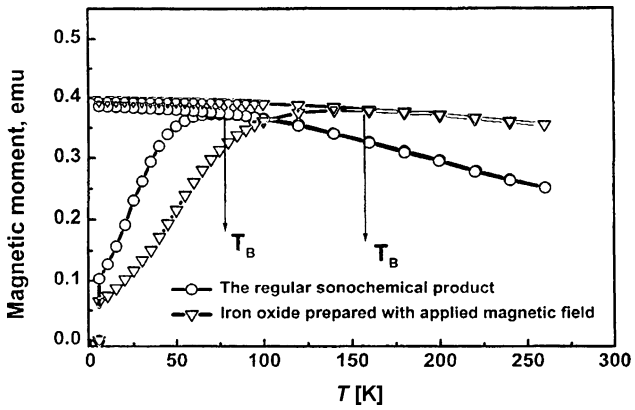

Figure 8. FC−ZFC magnetization curves for globular and acicular nanoparticles of amorphous Fe_2O_3 (Prozorov et al.[30]).

in an external magnetic field of 0.7 T.[30] The observed increase in the blocking temperature from 80 to 150 K was ascribed to the enhanced magnetic shape anisotropy of the acicular nanoparticles (Figure 8).

Magnetization measurements as a function of the magnetic field and temperature can significantly contribute to the complex qualitative (hysteretic/nonhysteretic behavior, saturation vs nonsaturation) and quantitative (values of coercive field (H_C), saturation magnetization (M_S), and remanent magnetization (M_R)) description of the magnetic behavior of the nanoscaled systems. At room temperature, the magnetization curves recorded for amorphous iron(III) oxide are not hysteretic and do not saturate, even at high applied fields (Figure 9).[20,27,28,36,47,70,74,83] Such behavior is in accordance with RT Mössbauer measurements and is expected in the unblocked regime of superparamagnetic particles, when the magnetic moment of particles can align in its various easy directions during measurement time. The simplest description of a superparamagnetic material in a magnetic field employing Boltzmann statistics is based on the following relation[92]

$$M = M_S\left(\coth\frac{\mu H}{kT} - \frac{kT}{\mu H}\right)$$

where the expression in parentheses represents the Langevin function, M is the total magnetic moment of particles per unit volume, μ is the magnetic moment of a single nanoparticle, M_S is the saturation magnetization, and k denotes the Boltzmann constant. As a result of the Langevin relationship, the saturation magnetization at a defined temperature is reached at a higher magnetic field for smaller particles. Such particle-size-dependent magnetic behavior was unambiguously proved for amorphous Fe_2O_3 nanopowders by Cao et al. (Figure 9A).[29] The decrease in the magnetization with decreasing particle size has been explained in terms of a non-collinear spin arrangement at or near the surface of the particle.[93,94] This particle size dependence is also valid for the nanocrystalline polymorphs of Fe_2O_3, but the magnetization curves clearly saturate.[20,23,74,84,85,91,95]

Below the blocking temperature, the magnetization cannot relax in the time window of the measurement, and a hysteretic (irreversible) behavior occurs (Figure 9B).[33,36,73,83] The nonsaturation behavior of the magnetization at a low temperature and under a high field proves that spins are randomly oriented as in spin-glass or cluster-spin-glass systems with competing exchange interactions below the spin freezing temperature.[33] As a result of the surface spin disorder, the hysteresis loop, after field cooling, is shifted for an amorphous Fe_2O_3 nanopowder prepared from Prussian Blue.[36] Such a shift in the magnetization

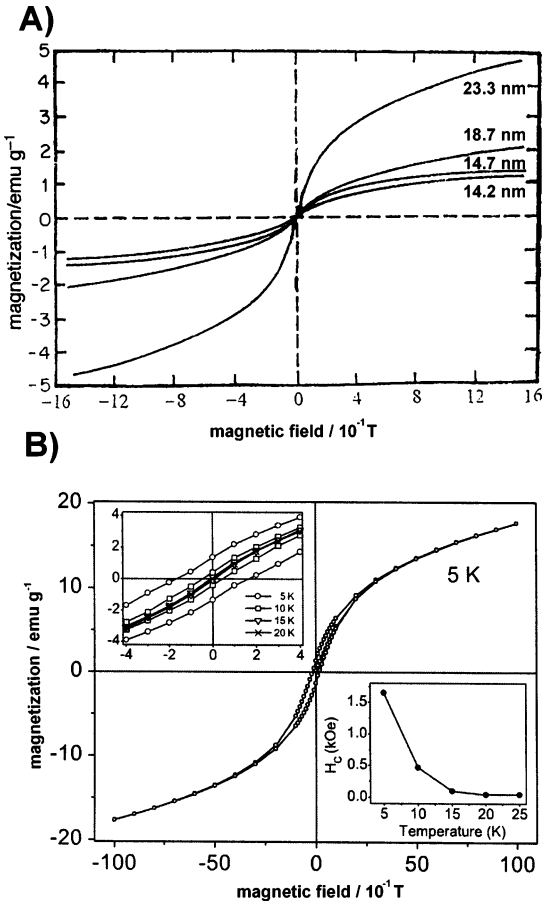

Figure 9. (A) Room temperature magnetization curves of amorphous Fe_2O_3 with different particle size (Cao et al.[29]). (B) Hysteresis loop for amorphous Fe_2O_3 nanopowder recorded at 5 K. The left inset shows the low-field region of the hysteresis loops measured at different temperatures. The right inset shows the temperature dependence of the coercive field H_C (Mukadam et al.[33]).

curve is usually exhibited by fine magnetic particles with spin-glass magnetic behavior. In such a model, below the transition temperature, the spin-glass surface shell creates an exchange field on the core of the particle, which is responsible for the observed shifted hysteresis loops.[90] In regard to the particle size dependence of the coercive field, it may be a bit complex for magnetic nanoparticles. Indeed, finite size effects reduce the coercive field but are often counterbalanced by surface effects that increase it. Such an increase of coercive field with decreasing particle size was observed for amorphous Fe_2O_3 nanopowders prepared from Prussian Blue,[36] and also for other nanometer-size systems including those consisting of iron oxide nanoparticles.[43,85,90,96−98]

4. Contribution of Other Experimental Techniques to the Characterization of Amorphous Fe_2O_3 Nanoparticles and to the Study of Their Crystallization Process

In addition to Mössbauer spectroscopy and various magnetic measurements, a long scale of other experimental techniques yielding important information on chemical purity, local structure, size, morphology, or thermal stability of amorphous Fe_2O_3 nanoparticles has been used by various authors.

X-ray powder diffraction (XRD) represents the most frequently used method for the verification of the amorphous nature of the sample. A flat line in the XRD pattern is a prerequisite for the absence of the periodic crystal lattice, and it also indicates that no parasitic crystalline compounds are contained in the

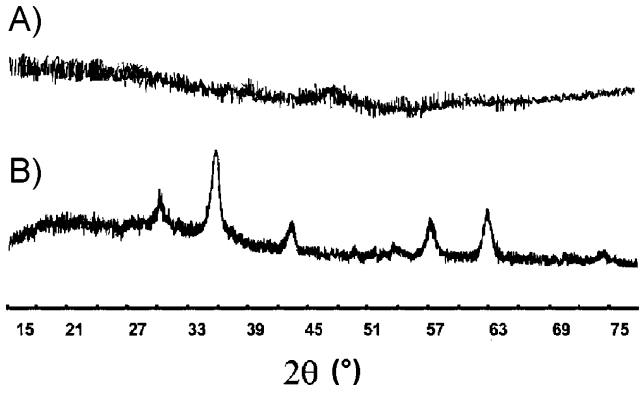

Figure 10. XRD patterns of amorphous (A) Fe_2O_3 and (B) nanocrystalline γ-Fe_2O_3 (Prozorov et al.[83]).

sample.[20,27,28,30,31,35,36,38,39,83] Thus, the absence of Bragg peaks in the XRD pattern is an important marker for the identification of amorphous Fe_2O_3 and its distinction from nanocrystalline Fe_2O_3 polymorphs, where broadened diffraction peaks usually appear (see Figure 10). However, the application of XRD for the detection of a real amorphous phase is limited if the samples contain the crystalline matrix or ultrasmall nanocrystalline "X-ray amorphous" polymorphs as the phase admixtures (see section 5). Possible distinguishing between amorphous phase and nanocrystalline Fe_2O_3 polymorphs is also dependent on the line resolution, which is determined by the wavelengths of the X-ray radiation (Mo, Cu, Co Kα).

In addition to the above-discussed Mössbauer spectroscopy, other spectroscopic techniques including infrared (IR), X-ray photoelectron (XPS), and electron paramagnetic resonance (EPR) spectroscopy were applied to monitor the electronic structure, chemical composition, and stoichiometry of an amorphous ferric oxide phase.[20,27,28,31,39,58] IR spectroscopy has been employed by various authors, particularly for the detection of the gaseous substances adsorbed on the surface of amorphous Fe_2O_3 particles.[20,27,28] XPS is one of the most powerful tools for obtaining information on the electronic structure and stoichiometry of solids. Thus, Palchik et al.,[31] who characterized amorphous ferric oxide prepared by pyrolysis of iron pentacarbonyl using XPS, confirmed a surprisingly good stoichiometry with an O−Fe ratio of 3.1:2. Moreover, a slight difference from the ideal value can be related to oxygen species adsorbed on the sample's surface in the form of water or carbonate. These oxygen species were identified in XPS spectra through the peaks at 532.3 and 533.5 eV. EPR measurements were taken on the amorphous Fe_2O_3−SiO_2 nanocomposites prepared by a sol−gel method.[39] Two main signals were resolved in the spectra and assigned to a bulk octahedral or tetrahedral site ($g \sim 2$) and a strongly distorted rhombic site located on the surface of the particle, in contact with the SiO_2 matrix ($g \sim 4.3$).[39] The position of the two lines is constant in the whole temperature range (see Figure 11), indicating the absence of an internal field, which is in good agreement with the magnetic measurements revealing a very low blocking temperature below 6 K. On the other hand, an acceptance of the possible tetrahedral positions in the local environment of Fe(III) contrasts with the Mössbauer data proving the octahedral surroundings.

The microscopic techniques, including TEM, high-resolution TEM (HRTEM), and AFM together with the Brunauer−Emmett−Teller (BET) surface area measurements, represent a group of experimental methods providing key information on the size, size distribution, morphology, and surface properties of amorphous Fe_2O_3 nanoparticles. TEM (HRTEM) analysis is the most frequently used, although its objectivity and applicabil-

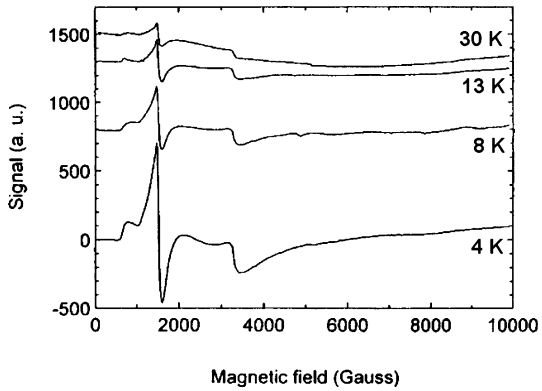

Figure 11. X-band EPR spectra of amorphous Fe_2O_3 dispersed in a silica matrix recorded between 4 and 30 K (Ennas et al.[39]).

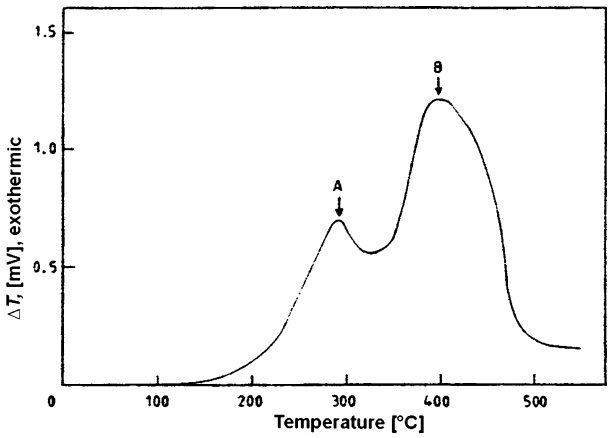

Figure 12. DTA of the amorphous Fe_2O_3 nanopowder synthesized by the three-component microemulsion technique (Ayyub et al.[34]).

ity are partially restricted due to the difficulty in sample preparation resulting rather in the imaging of large agglomerates than separated particles.[20,27,28,30,31,39,83] Thus, it is questionable whether the relatively large objects observed in TEM micrographs of amorphous ferric oxide samples with diameters of a few tens of nanometers[20,29,83] represent the real particles or if they correspond to the agglomerates comprised of ultrasmall amorphous particles. At this point, and following the analyses of various data on amorphous Fe_2O_3, we emphasize that its amorphicity is related to an ultrasmall dimension and "space restriction", leading to the absence of a periodic lattice. From this viewpoint, the use of transmission electron microscopy to verify the character of the amorphous sample is also a crucial point, as the crystallization process can occur under an electron beam. This drawback can be eliminated if nondestructive atomic force microscopy is applied.[26,36] It offers very precise information on the vertical dimensions of particles, and the sample preparation also allows the imaging of the well-separated particles (see Figure 5B). On the other hand, the values of the lateral dimensions are strongly affected due to the "tip−sample surface" convolution, and thus, the obtained morphological information is very poor. As an indirect tool for the evaluation of the particle size, BET surface area measurements could be realized if general assumptions of globular particle shape, nonporous sample character, and narrow size distribution are fulfilled.[36] In the case of the porous sample, the existence and the volume of the pores, together with their size distribution, can be determined from BET measurements (see Figure 1).[20]

Thermal analyses, including thermogravimetry (TG), differential thermal analysis (DTA), and differential scanning calorimetry (DSC), significantly contribute to an explanation of the crystallization mechanism of amorphous iron(III) oxide.[27−31,34,83] Table 3 summarizes the results concerning the crystallization mechanism of amorphous iron(III) oxide published by various authors.

They will be discussed with respect to the role of crystallization atmosphere, temperature, sample character, and particle size, all of which are the principal factors influencing the structure of the primarily formed crystalline phase.

It is evident that nanocrystalline maghemite is the primary crystallization product if nanopowdered amorphous Fe_2O_3 is heated under air, in full accordance with the conclusions of the majority of the authors.[28,30,31,34,36,83] As indirect evidence, two well-resolved exothermic peaks can be observed in the DTA and DSC curves of amorphous ferric oxide nanopowder. To illustrate, the DTA curve for amorphous iron(III) oxide prepared by a microemulsion technique[34] is shown in Figure 12. The first exothermic peak observed at 292 °C can be attributed to the process of crystallization of amorphous Fe_2O_3 to γ-Fe_2O_3, while the other one, being more intensive and occurring at 396 °C, corresponds to the polymorphous isochemical transformation of γ-Fe_2O_3 to α-Fe_2O_3. The studied phase transitions were found to be irreversible, and thus, the rescanned DTA curve after the cooling of the sample revealed none of the described effects, indicating the presence of thermally stable hematite.

The thermally induced transformation process of amorphous $Fe_2O_3-SiO_2$ nanocomposites under air yields the same primary crystallization product as in the case of nanopowdered samples, with the only difference being a significantly higher crystal-

TABLE 3: Summary of Data on the Thermally Induced Crystallization of Amorphous Iron(III) Oxide under Various Conditions[a]

author	particle size of amorphous Fe_2O_3 (nm)	atmosphere	T_c (°C)	product of crystallization	form
Liao[27]	3−5	air	340	α-Fe_2O_3	nanopowder
Subrt[32]	200 m^2/g (specific surface area)	air	450−500	∗	nanopowder
Cao[28]	25	air	268	γ-Fe_2O_3	nanopowder
Cao[29]	23.3	nitrogen	280	Fe_3O_4	nanopowder
	18.7	nitrogen	277	Fe_3O_4	nanopowder
	14.7	nitrogen	290	Fe_3O_4	nanopowder
	14.2	nitrogen	298	Fe_3O_4	nanopowder
Palchik[31]	2-3	air	250	γ Fe_2O_3	nanopowder
	2-3	vacuum	500	α-Fe_2O_3	nanopowder
Ayyub[34]	5	air	292	γ-Fe_2O_3	nanopowder
Zboril[36]	1.5−2.5	air	280	γ-Fe_2O_3	nanopowder
Cannas[38]	4−6	air	700	γ-Fe_2O_3	nanocomposite
Diepen[46]	∗	air	250	β-Fe_2O_3, α-Fe_2O_3	layer
Heiman[49]	∗	air	500	∗	film
Ennas[39]	3−4	air	700	γ-Fe_2O_3	nanocomposite

[a] T_c, crystallization temperature; ∗, the authors do not specify the crystallization product.

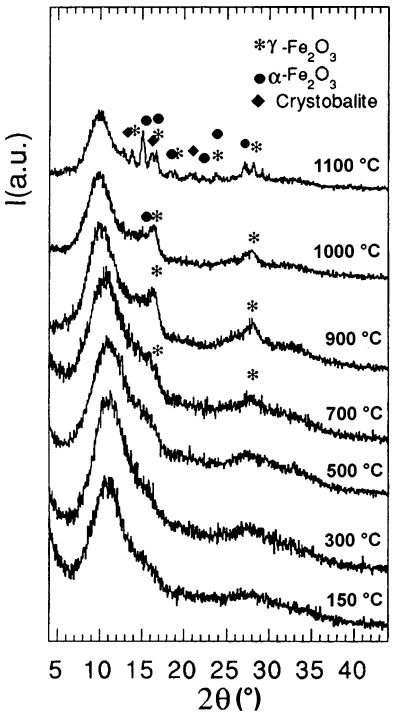

Figure 13. XRD patterns of samples prepared by thermal treatment of amorphous $Fe_2O_3-SiO_2$ nanocomposite at various temperatures in air (Ennas et al.[39]).

lization temperature (700 °C), expected due to the preventive role of the matrix.[38,39] The process of crystallization of an amorphous $Fe_2O_3-SiO_2$ nanocomposite at various temperatures under air is manifested by XRD patterns in Figure 13. Only the most intensive peaks of maghemite are visible in the XRD patterns of samples heated at temperatures below 1000 °C, while hematite appears at higher temperatures together with crystobalite, which is formed by the crystallization of the amorphous SiO_2 matrix.

In regard to amorphous Fe_2O_3 films and layers, β-Fe_2O_3 and α-Fe_2O_3 were identified as the crystallization products.[46] However, the literature data in this field are very poor.

Cao et al. carried out a complex study of the crystallization process of amorphous Fe_2O_3 nanopowder under an inert atmosphere (N_2) using XRD, magnetization measurements, DSC, TG, and magnetic TG measurements.[29] On the basis of complementary experimental results, magnetite (Fe_3O_4) was determined as the direct crystallization product of an amorphous ferric oxide phase in nitrogen. Unfortunately, the identification of magnetite from XRD and magnetization measurements is moot due to the structural and magnetic similarity of magnetite to maghemite. Nevertheless, TG measurements realized in an applied magnetic field (Figure 14a) and under a nitrogen atmosphere provide strong support for the primary formation of a magnetite phase. The mass loss observed in the magnetic TG curve of amorphous Fe_2O_3 at about 300 °C (curve 1) was ascribed to the conversion of Fe_2O_3 to Fe_3O_4. The mass increase between 300 and 500 °C is related to the presence of a strong magnetic phase (Fe_3O_4) in the system, while the final mass loss above 500 °C corresponds to the transition of magnetite from a ferrimagnetic to a paramagnetic state, which is completed around the Curie point of magnetite (570 °C). Curve 2 in Figure 14a displays the magnetic TG curve of the amorphous Fe_2O_3 sample previously heated up to 900 °C in nitrogen. As can be clearly seen, the shape of the curve and its character are in agreement with those of commercial Fe_3O_4 (curve 3 in Figure 14a).

The effect of the particle size of the amorphous ferric oxide phase on the crystallization temperature was investigated by the same authors using DSC.[29] Four samples were prepared by a sonochemical method using $Fe(CO)_5$ as a precursor, and their particle size was controlled through a change in iron pentacarbonyl concentration. Samples having different surface areas of 79, 148, 181, and 207 m^2/g, reflecting differences in particle dimensions, were assigned as A, B, C, and D, respectively. Generally, their DSC curves recorded under a nitrogen atmosphere (Figure 14b) exhibit an endothermic peak at approximately 150 °C, which is attributed to a desorption of contaminants and gaseous phases from the surface of the particles. The large exothermic effect is assigned as a manifestation of the crystallization of amorphous Fe_2O_3. Obviously, the crystallization temperature increases with the decreasing particle size from 280 °C for sample A to 298 °C for sample D.

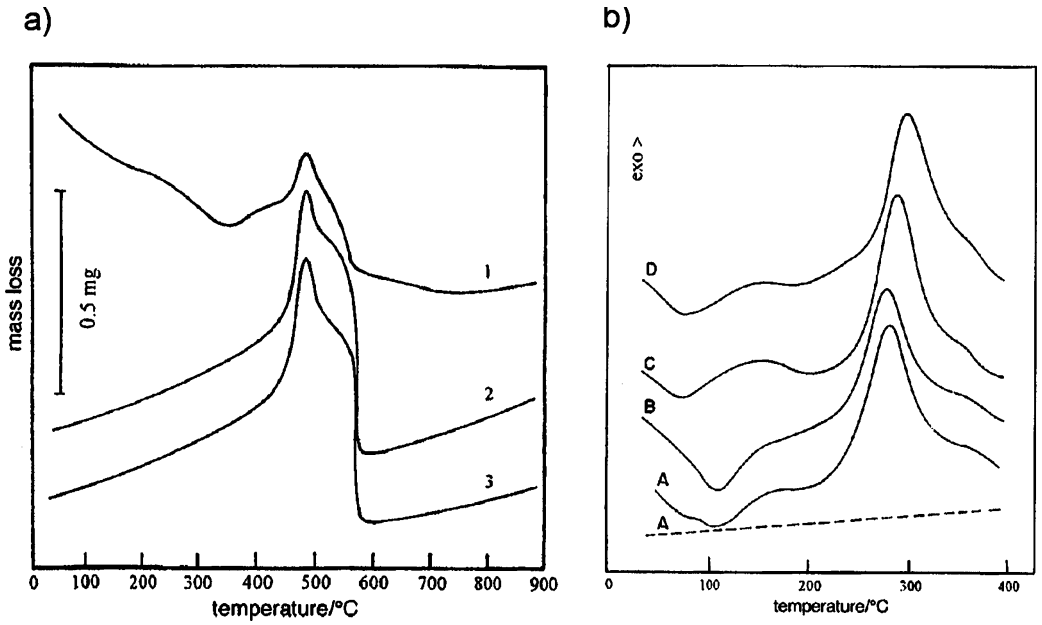

Figure 14. (a) Magnetic TG curves of amorphous Fe_2O_3 nanopowder before heat treatment (1) and after heating to 900 °C under nitrogen (2) and of commercial Fe_3O_4 (3). (b) DSC curves of amorphous Fe_2O_3 nanopowders with the average size decreasing in the sequence A, B, C, D, respectively (solid lines), and DSC curve after previous heating to 400 °C (dashed line). All curves were recorded under a nitrogen atmosphere (Cao et al.[29]).

It is worth mentioning here that there are almost no literature data concerning the thermal behavior of amorphous iron(III) oxide in the reduction atmospheres. However, it was recently found to be a suitable precursor for solid-state synthesis in a hydrogen atmosphere, leading to larger magnetic nanoparticles with a narrow size distribution. Thus, the magnetic composites of α-Fe and/or Fe_3O_4 nanoparticles dispersed in a MgO matrix were prepared by the controlled thermal reduction of amorphous Fe_2O_3 nanopowder with nanocrystalline Mg under a hydrogen atmosphere.[99] The excellent magnetic properties of nanoparticles, combined with a low molar weight, biocompatibility, and high chemical and thermal stability of the nanocrystalline MgO matrix, make the prepared nanocomposites applicable in various processes including biomagnetic separations.

5. Amorphous versus Nanocrystalline Fe_2O_3

From the previous sections, one can conclude that it is very difficult to distinguish experimentally between a true amorphous Fe_2O_3 phase and nanocrystalline polymorphs exhibiting very small particle size. Similarly, the quantification of the relative proportions of amorphous and nanocrystalline fractions is a crucial issue. There are two diffraction techniques yielding direct structural information: X-ray powder diffraction (XRD) and selected area electron diffraction (SAED) as part of TEM analysis. If the (nano)crystalline phase is present in the sample, its principal diffraction lines should be resolved in an XRD pattern (see Figure 10), although they are usually significantly broadened or can grow from the amorphous background. As the key point, XRD gives only limited information if very small particles (below 5 nm) are analyzed, when the patterns reveal largely an undulating background. As a result, it is almost impossible to resolve and quantify the content of true amorphous and nanocrystalline X-ray amorphous Fe_2O_3 phases. Moreover, the applicability of XRD analysis for distinguishing amorphous and nanocrystalline iron(III) oxide phases is restricted in the case of nanocomposite samples with a crystalline matrix and a low content of Fe_2O_3 nanoparticles. This problem is also encountered in SAED analysis. Nevertheless, the amorphous SAED pattern is clear evidence for the presence of an amorphous phase because of the absence of any diffraction rings (see Figure 4). However, it is necessary to take into account that this indication of amorphicity is usually related to a very low number of particles involved in such an analysis.

An indirect approach emerging from the monitoring of thermal and magnetic behavior is applicable, but the obtained data are strongly affected by the sample character and the measurement conditions. As mentioned in section 4, the thermally induced crystallization mechanism is still a controversial subject and very different primary crystallization products can be identified depending on the atmosphere, heating conditions (isothermal vs dynamic treatment), sample weight, material thickness, and sample character (layer, powder, composite). Even in an "ideal" case, when crystallization occurs under air in two steps via maghemite to hematite (see DTA in Figure 12), we have no information on the content of the amorphous phase, as two exoeffects can be observed both for the completely amorphous Fe_2O_3 and for the sample with its negligible concentration.

In regard to the magnetic response to the presence of amorphous iron(III) oxide in the sample, there are again several problems with its unambiguous detection. This is mainly due to the key role of surface effects and interparticle interactions, which can manifest themselves in the same way in an assembly of both amorphous and nanocrystalline Fe_2O_3 particles. Thus, we cannot draw any conclusion about the presence of the amorphous phase from the temperature dependence of magnetization from FC−ZFC curves (including values of the magnetic transition—T_B, T_f) and from the width of the magnetic transition, as these characteristics (see section 3) can be very similar. They can also be similar for ultrasmall maghemite particles, mainly if we consider the powdered samples with a high degree of interparticle interaction.[89,100] On the other hand, there are some "magnetic markers", allowing the direct identification of the amorphous Fe_2O_3 phase independently of the sample's character. Important information can be extracted mainly from the value of saturation magnetization (M_S) and/or, if the hysteresis loop does not saturate, from the magnetization at a maximum applied field (M_{max}), which is considerably reduced in amorphous Fe_2O_3 samples compared to nanocrystalline maghemite, γ-Fe_2O_3. To be more specific, the values of M_{max}, recorded from hysteresis loops at 5 K in an applied field of 10 T, are for amorphous Fe_2O_3 nanopowders lower than 20 emu/g,[33,36,73] while nanopowdered maghemite shows, under the same conditions, significantly higher values ranging from 50 to 90 emu/g, depending on the particle size.[85,101−107] Even very small 3-nm-sized maghemite particles exhibit incomparably higher M_{max} (≈50 emu/g)[108] than amorphous particles of almost the same size.[33,36,73] It is worth mentioning that nanocrystalline hematite (α-Fe_2O_3), being a representative of antiferromagnetic compounds, shows a very low value of M_S (1−2.5 emu/g)[109,110] and thus its magnetic distinction from amorphous Fe_2O_3 is also very easy. The application of the M_S and M_{max} values as markers for distinguishing amorphous Fe_2O_3 from maghemite and/or hematite is partially complicated in the case of the Fe_2O_3 nanocomposites with some matrix, where these magnetic parameters are usually reported for the whole composite.[43] In such a case, it is necessary to take into account the weight ratio of a magnetic Fe_2O_3 fraction to a nonmagnetic matrix to decide on the amorphicity of Fe_2O_3 from the reduced value of the saturation magnetization.

Two other magnetic markers of the amorphous phase are extractable from Mössbauer spectra measured at the lowest temperatures and in sufficiently high external magnetic fields. The first is the value of the hyperfine magnetic field (B_{hf}), usually registered at liquid helium temperature (T_{He}), which is drastically reduced compared to that found for nanocrystalline maghemite and hematite samples. Although the spectra of amorphous Fe_2O_3 recorded at T_{He} are usually fitted by a distribution of hyperfine magnetic fields, the determined average fields vary from 45 T for the nanocomposite with a low degree of interparticle interaction,[78] via 47 T in the case of an amorphous film,[46,47,49,50] to 49 T for the nanopowdered sample.[34,36] Nevertheless, these values are incomparably lower than those reported for nanocrystalline hematite samples (51−54 T).[111,112] Similarly, a Mössbauer spectrum of nanomaghemite at T_{He} possesses a larger B_{hf} (≈50−51 T) than the amorphous phase, mainly if it is fitted by one sextet due to the strong overlapping of tetrahedral and octahedral subspectra.[113−115] If the contributions of both sublattices in the spinel structure of maghemite are resolved in the spectrum, the high value of B_{hf} corresponding to octahedral Fe(III) ions (≈51.5−52.5 T)[116] represents an important parameter allowing a distinction from the amorphous phase.

The second Mössbauer marker, enabling the distinction of an amorphous Fe_2O_3 phase from nanocrystalline maghemite and hematite, is based on its specific magnetic behavior in an external magnetic field. It is known that in a random distribution of the magnetic moments within the particle and in a zero-applied field, the intensity ratio of the six lines of the magnetically split Mössbauer spectra is 3:2:1:1:2:3. In most

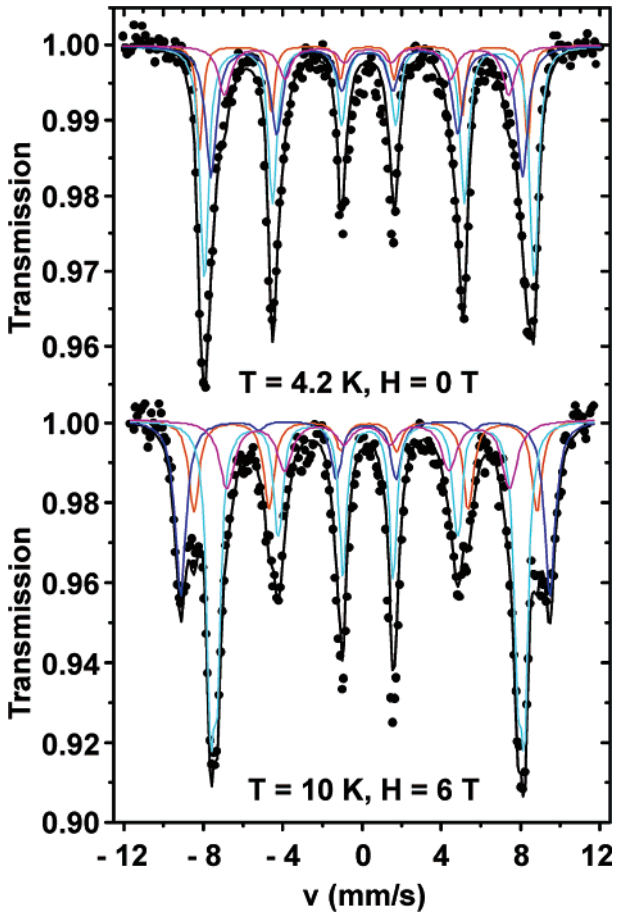

Figure 15. Zero-field (4.2 K/0 T) and in-field (10 K/6 T) Mössbauer spectra of a mixture of α-Fe_2O_3, γ-Fe_2O_3, and amorphous Fe_2O_3 nanoparticles prepared by the sol−gel method, where corresponding subspectra are denoted by different colors: violet, amorphous Fe_2O_3; brown, α-Fe_2O_3; dark blue, tetrahedral site of γ-Fe_2O_3; light blue, octahedral site of γ-Fe_2O_3 (Casas et al.[78]).

cases, when the studied magnetic sample is exposed to the applied magnetic field, the magnetic moments of the atoms respond to it by a rearrangement of their orientations, which is then reflected by a change in the line intensities in the Mössbauer spectrum.[117] In particular, if the direction of the external magnetic field is parallel to that of the propagation of gamma rays, then the second and fifth lines of the Mössbauer spectrum vanish from well-crystalline ferromagnetic and/or ferrimagnetic materials, including maghemite, thus giving an intensity ratio of 3:0:1:1:0:3.[54] This reflects the perfect alignment of the magnetic moments to a parallel and/or antiparallel direction to the applied magnetic field, making an angle of 0 and/or 180° with the direction of gamma rays. Moreover, an external magnetic field provokes the clear separation of the spectral contributions from the nonequivalent structural sublattices in the ferrimagnetic compounds. For antiferromagnetic samples, including hematite, with a low magnetic anisotropy, the in-field Mössbauer spectra provide useful information only when recorded above the critical field, which is characteristic of a particular compound, above which a sharp spin reorientation occurs as the directions of all the magnetic moments flip to a plane perpendicular to the direction of propagation of gamma rays. This is manifested by an enhancement of intensities of the second and fifth lines, resulting in an ideal ratio of 3:4:1:1:4:3.[118,119] However, it should be stressed that deviations from the ideal ratios of the line intensities can be observed, especially in nanocrystalline samples possessing a high degree of spin frustration. Nevertheless, a remarkable change in zero-field and external-field Mössbauer spectra of maghemite and hematite is the principal difference in comparison with amorphous Fe_2O_3, exhibiting no change in the line intensities (see section 3.1)

To demonstrate the applicability of a "Mössbuaer marker" for the identification and quantification of the amorphous fraction in the phase mixture with nanocrystalline polymorphs, we present low-temperature zero-field and in-field Mössbauer spectra, including their hyperfine parameters (see Figure 15 and Table 4), for the Fe_2O_3−SiO_2 nanocomposite sample prepared by the sol−gel method.[78] The in-field spectrum was recorded in an external magnetic field applied parallel to the direction of gamma rays. XRD analysis of such a material indicates the presence of γ-Fe_2O_3 and α-Fe_2O_3 nanoparticles with a mean diameter of about 8 nm. However, the contribution of the amorphous phase can not be excluded. Moreover, by the synthetic route used, it is difficult to evaluate the quantity of iron (molar ratio of Fe−Si) that has precipitated inside the SiO_2 gel. In such a complicated system, the application of other techniques, including magnetic measurements for the detection or even quantification of the amorphous phase, is considerably restricted. On the other hand, Mössbauer spectroscopy allows the identification and quantification of the fraction of amorphous Fe_2O_3, even from a low-temperature spectrum (see Figure 15, top). From the parameters listed in Table 4, this is possible mainly due to the above-mentioned reduced hyperfine magnetic field (45.0 T) of the amorphous phase, which is significantly lower than those of the values corresponding to α-Fe_2O_3 (50.7 T) and both structural positions in γ-Fe_2O_3 (48.8; 51.6 T—see Table 4). A better distinction between all of the phases is achieved from an in-field spectrum (see Figure 15, bottom), where the sublattices corresponding to the tetrahedral A (dark blue line) and octahedral B (light blue line) positions in maghemite are better separated as the observed isomer shift parameters (A, 0.43 mm/s; B, 0.53 mm/s) and effective magnetic fields (B_{eff}) (A, 57.6 T; B, 47.8 T) differ more significantly (see

TABLE 4: Hyperfine Parameters Deduced from the Zero-Field and In-Field Mössbauer Spectra of the Iron(III) Oxide Nanoparticles Hosted in Silica Aerogel (Taken from Casas et al.[78])[a]

T (K)/B_{ext} (T)	iron oxide	δ_{Fe} (mm/s) (±0.02)	2ϵ (mm/s) (±0.02)	B_{eff} (T) (±0.04)	B_{hf} (T) (±0.04)	β (deg)	RA (%) (±2)
4.2 K/0 T	α-Fe_2O_3	0.45	−0.17		50.7		16
	γ-Fe_2O_3	0.42	0.03		48.8		20
	γ-Fe_2O_3	0.51	0.03		51.6		40
	Am-Fe_2O_3	0.45	0.05		45.0		24
10 K/6 T	α-Fe_2O_3	0.46	−0.17	54.0	52.3	76	12
	γ-Fe_2O_3	0.43	-0.04	57.6	51.7	8	20
	γ-Fe_2O_3	0.53	-0.02	47.8	52.8	36	44
	Am-Fe_2O_3	0.47	0.00		44.6*		24

[a] δ_{Fe}, isomer shift relative to metallic iron; 2ϵ, quadrupole shift; B_{ext}, external magnetic field; B_{eff}, effective magnetic field; B_{hf}, hyperfine magnetic field; $\mathbf{B}_{eff} = \mathbf{B}_{ext} + \mathbf{B}_{hf}$; β, angle between the direction of Fe magnetic moments and the γ-beam; RA, relative subspectrum area; *, the Mössbauer component was adjusted with a speromagnetic model.

Table 4). Moreover, the ferrimagnetic behavior of maghemite is reflected in the in-field spectrum through the reduced intensities of the second and fifth spectral lines, although the nanocrystalline character of particles (the spin frustration effect) causes these lines do not completely vanish as expected in an ideal case. Similarly, the subspectrum of hematite (brown line) is clearly distinguished through the value of B_{eff} (54.0 T) and increased intensities of lines 2 and 5, which again differ somewhat from the theoretical values (3:4:1:1:4:3) for the antiferromagnetic phase due to the nanoparticle nature. Most importantly, the amorphous Fe_2O_3 phase is easily detectable in the in-field spectrum, as its subspectrum (violet line) does not reveal any change in the line intensities compared to the zero-field spectrum, and the observed value of magnetic splitting remains considerably reduced (44.6 T).

To summarize, the saturation value of the hyperfine magnetic field and the unchanged intensities of the spectral lines in zero-field and in-field Mössbauer spectra are excellent magnetic markers for identifying the amorphous Fe_2O_3 phase. In the mixture with nanocrystalline polymorphs, it can be unambiguously distinguished and quantified from the corresponding spectrum area. Moreover, thanks to the element selectivity of Mössbauer spectroscopy, these markers have a universal character and are applicable for monitoring the amorphous iron(III) oxide phase both in the powdered form and in the composite.

6. Summary and Outlook

In this short review, amorphous Fe_2O_3 is presented as an advanced material applicable in various fields of modern nanotechnologies, including catalysis, optical and humidity sensors, or magnetic fluids. Due to its superior electrochemical, sorption, magnetic, optical, and other properties, the great boom in the development of new syntheses towards amorphous ferric oxide occurred in the last few years. These preparation routes are summarized and classified according to the nature and properties of the material and their advantages, together with their drawbacks. The interesting magnetic behavior is monitored by a view of Mössbauer spectroscopy and magnetic measurements. The significantly reduced values of saturation magnetization, effective magnetic moment, and the hyperfine magnetic field at liquid helium temperature, and a negligible change between low-temperature zero-field and in-field Mössabuer spectra, are not only the results of the specific magnetism of amorphous Fe_2O_3 but also the key markers for its being identified and distinguished from the nanocrystalline polymorphs. The reflections of the particle size, morphology, and interparticle interactions in the magnetization and FC−ZFC curves are explored to describe the magnetic regime of variously prepared amorphous samples. With an increasing degree of interparticle interaction, the shift in the magnetic behavior from the superparamagnetic to the spin-glass-like state is obvious. The collected literature data also agree on maghemite (γ-Fe_2O_3) as a primary crystallization product if amorphous ferric oxide is heated under air, although the crystallization temperature varies depending on the particle size. On the other hand, the data concerning the mechanism of thermally induced transformation to a crystalline state under inert and reduction atmospheres are very poor and unclear, indicating the possible primary formation of magnetite (Fe_3O_4), maghemite, and hematite (α-Fe_2O_3). There are also many other controversial points, which should be explained in the near future. They are related especially to the description of the magnetic regime below the ordering temperature of amorphous nanoparticles. Which type of ordering do amorphous nanoparticles exhibit there? Is a speromagnetic model universally applicable for such a purpose? Similarly, the structure of the neighboring environment of Fe(III) in an amorphous ferric oxide phase is still a subject of discussion. A general accord on the octahedral environment, confirmed by various techniques, contrasts with the structure of maghemite as the primary crystallization phase containing tetrahedral positions in the spinel lattice. According to the opinion of the authors, the reason for this can be inherent in the symmetry of the surrounding iron being maximal in both positions of the maghemite structure, similar to that in amorphous ferric oxide, which is clearly proven by low-temperature Mössbauer spectroscopy. From the experimental viewpoint, the use of microscopic techniques for the evaluation of the structure and size of amorphous particles seems to be a questionable issue, as TEM or HRTEM can induce sample crystallization under an electron beam, and the application of atomic force microscopy is strongly limited at such low particle dimensions due to the tip−particle surface convolution.

Acknowledgment. This work was supported by the Projects of the Ministry of Education of the Czech Republic (1M-6198959201; MSM6198959218). The authors also gratefully thank Jiri Tucek (Palacky University Olomouc, Czech Republic) for the final corrections of the manuscript.

References and Notes

(1) Chan, H. B. S; Ellis, B. L. *Adv. Mater.* **2004**, *16*, 144.
(2) Li, W. Z.; Xie, S. S.; Qian, L. X.; Chang, B. H.; Zou, B. S.; Zhou, W. Y.; Zhao, R. A.; Wang, G. *Science* **1996**, *274*, 1701.
(3) Xie, S. S.; Chang, B. H.; Li, W. Z.; Pan, Z. W.; Sun, L. F.; Mao, J. M.; Chen, X. H.; Qian, L. X.; Zhou, W. Y. *Adv. Mater.* **1999**, *11*, 1135.
(4) Hou, H. Q.; Schaper, A. K.; Weller, F.; Greiner, A. *Chem. Mater.* **2002**, *14*, 3990.
(5) Ensling, J.; Gütlich, P.; Klinger, R.; Meisel, W.; Jachow, H.; Schwab, H. *Hyperfine Interact.* **1998**, *111*, 143.
(6) Teng, X. W.; Black, D.; Watkins, N. J.; Gao, Y. L.; Yang, H. *Nano Lett.* **2003**, *3*, 261.
(7) Depeyrot, J.; Sousa, E. C.; Aquino, R.; Tourinho, F. A.; Dubois, E.; Bacri, J.-C.; Perzynski, R. *J. Magn. Magn. Mater.* **2000**, 252, 375.
(8) Zayat, M. Z.; del Monte, F.; Morales, M. D.; Rosa, G.; Guerrero, H.; Serna, C. J.; Levy, D. *Adv. Mater.* **2003**, *15*, 1809.
(9) Tejada, J.; Ziolo, R. F.; Zhang, X. X. *Chem. Mater.* **1996**, *8*, 1784.
(10) Mitchell, D. G. *Magn. Reson. Imaging* **1997**, *7*, 1.
(11) McMichael, R. D.; Schull, R. D.; Swartzendruber, L. J.; Bennett, L. H.; Watson, R. E. *J. Magn. Magn. Mater.* **1992**, *111*, 29.
(12) Josephson, L.; Tsung, C. H.; Moore, A.; Weissleder, R. *Bioconjugate Chem.* **1999**, *10*, 186.
(13) Nagano, H.; Machida, Y.; Iwata, M.; Imada, T.; Noguchi, Y.; Matsumoto, A.; Nagai, T. *Int. J. Pharm.* **1997**, *147*, 119.
(14) Spiers, K. M.; Cashion, J. D.; Gross, K. A. *Key Eng. Mater.* **2004**, *254−2*, 213.
(15) Danzfuss, B.; Stimming, U. *J. Electroanal. Chem.* **1984**, *164*, 89.
(16) Murawski, L.; Chung, C. H.; Mackenzie, J. D. *J. Non-Cryst. Solids* **1979**, *32*, 91.
(17) Sarradin, J.; Guessous, A.; Ribes, M. *J. Power Sources* **1996**, *62*, 149.
(18) Wohlfarth, E. P., Ed. *Ferromagnetic materials*; North-Holland: Amsterdam, The Netherlands, 1980; Vol. 2, p 405.
(19) Perkas, N.; Koltypin, Yu.; Palchik, O.; Gedanken, A.; Chandrasekaran, S. *Appl. Catal., A* **2001**, *209*, 125.
(20) Srivastava, D. N.; Perkas, N.; Gedanken, A.; Felner, I. *J. Phys. Chem. B* **2002**, *106*, 1878.
(21) Ren, P. C.; Tan, Z. K.; Luo, W. X. *Chin. J. Chem. Eng.* **1996**, *4*, 264.
(22) Shafi, K. V. P. M.; Wizel, S.; Prozorov, T.; Gedanken, A. *Thin Solid Films* **1998**, *318*, 38.
(23) Casas, L.; Roig, A.; Rodriguez, E.; Molins, E.; Tejada, J.; Sort, J. *J. Non-Cryst. Solids* **2001**, *285*, 37.
(24) Jain, G.; Capozzi, C. J.; Xu, J. J. *J. Electrochem. Soc.* **2003**, *150*, A806.
(25) Neri, G.; Bonavita, A.; Milone, C.; Pistone, A.; Galvagno, S. *Sens. Actuators, B* **2003**, *92*, 326.
(26) Prabhakaran, K.; Shafi, K. V. P. M. *Adv. Mater.* **2001**, *13*, 1859.
(27) Liao, X.; Zhu, J.; Zhong, W.; Chen, H. Y. *Mater. Lett.* **2000**, *50*, 341.

(28) Cao, X.; Prozorov, R.; Koltypin, Yu.; Kataby, G.; Felner, I.; Gedanken, A. *J. Mater. Res.* **1997**, *12*, 402.
(29) Cao, X.; Koltypin, Yu.; Prozorov, R.; Kataby, G.; Gedanken, A. *J. Mater. Res.* **1997**, *7*, 2447.
(30) Prozorov, T.; Prozorov, R.; Koltypin, Yu.; Felner, I.; Gedanken, A. *J. Phys. Chem. B* **1998**, *102*, 10165.
(31) Palchik, O.; Felner, I.; Kataby, G.; Gedanken, A. *J. Mater. Res.* **2000**, *15*, 2176.
(32) Subrt, J.; Bohacek, J.; Stengl, V.; Grygar, T.; Bezdicka, P. *Mater. Res. Bull.* **1998**, *34*, 905.
(33) Mukadam, M. D.; Yusuf, S. M.; Sharma, P.; Kulshreshtha, S. K. *J. Magn. Magn. Mater.* **2004**, *269*, 317.
(34) Ayyub, P.; Multani, M.; Barma, M.; Palkar, V. R.; Vijayaraghavan, R. *J. Phys. C: Solid State Phys.* **1988**, *21*, 2229.
(35) Kan, S. H.; Yu, S.; Peng, X. G.; Zhang, X. T.; Li, D. M.; Xiao, L. Z.; Zou, G. T.; Li, T. J. *J. Colloid Interface Sci.* **1996**, *178*, 673.
(36) Zboril, R.; Machala, L.; Mashlan, M.; Sharma, V. *Cryst. Growth Des.* **2004**, *4*, 1317.
(37) Tanaka, K.; Kamyia, K.; Matsuoka, M.; Yoko, T. *J. Non-Cryst. Solids* **1987**, *94*, 365.
(38) Cannas, C.; Concas, G.; Musinu, A.; Piccaluga, G.; Spano, G. *Z. Naturforsch., A: Phys. Sci.* **1999**, *54*, 513.
(39) Ennas, G.; Musinu, A.; Piccaluga, G.; Zedda, D.; Gatteschi, D.; Sangregorio, C.; Stanger, J. L.; Concas, G.; Spano, G. *Chem. Mater.* **1998**, *10*, 495.
(40) Hrianca, I.; Caizer, C.; Savii, C.; Popovici, M. *J. Optoelectron. Adv. Mater.* **2000**, *2*, 634.
(41) Concas, G.; Ennas, G.; Gatteschi, D.; Musinu, A.; Piccaluga, G.; Sangrgorio, C.; Spano, G.; Stanger, J. L.; Zedda, D. *Chem. Mater.* **1998**, *10*, 495.
(42) Casu, M.; Marincola, F. C.; Lai, A.; Musinu, A.; Piccaluga, G. *J. Non-Cryst. Solids* **1998**, *232-234*, 329.
(43) Cannas, C.; Gatteschi, D.; Musinu, A.; Piccaluga, G.; Sangrgorio, C. *J. Phys. Chem. B* **1998**, *102*, 7721.
(44) Bruni, S.; Cariati, F.; Casu, M.; Lai, A.; Musinu, A.; Piccaluga, G.; Solinas, S. *Nanostruct. Mater.* **1999**, *11*, 573.
(45) Cannas, C.; Concas, G.; Falqui, A.; Musinu, A.; Spano, G.; Piccaluga, G. *J. Non-Cryst. Solids* **2001**, *286*, 64.
(46) van Diepen, A. M.; Popma, Th. J. A. *Solid State Commun.* **1978**, *27*, 121.
(47) van Diepen, A. M.; Popma, T. J. A. *J. Phys., Colloque* **1976**, *37*, C6-755.
(48) Zotti, G.; Schiavon, G.; Zecchin, S. *J. Electrochem. Soc.* **1998**, *145*, 385.
(49) Heiman, N.; Kazama, N. S. *J. Appl. Phys.* **1979**, *50*, 7633.
(50) Howard, D. G.; Nussbaum, R. H. *Surf. Sci.* **1980**, *93*, L105.
(51) Zhong, Z. Y.; Zhao, Y. M.; Koltypin, Y.; Gedanken, A. *J. Mater. Chem.* **1998**, *8*, 2167.
(52) Kataby, G.; Prozorov, T.; Koltypin, Y.; Cohen, H.; Sukenik, C. N.; Ulman, A.; Gedanken, A. *Langmuir* **1997**, *13*, 6151.
(53) Zboril, R.; Mashlan, M.; Petridis, D. *Chem. Mater.* **2002**, *14*, 969.
(54) Tuček, J.; Zboril, R.; Petridis, D. *J. Nanosci. Nanotechnol.* **2006**, *6*, 926.
(55) Zboril, R.; Mashlan, M.; Barcova, K.; Vujtek, M. *Hyperfine Interact.* **2002**, *139*, 597.
(56) Bourlinos, A.; Zboril, R.; Petridis, D. *Microporous Mesoporous Mater.* **2003**, *58*, 155.
(57) Sivakumar, M.; Gedanken, A. *Ultrason. Sonochem.* **2004**, *11*, 373.
(58) Li, X.; Lin, E.; Zhang, C.; Li, S. *J. Mater. Chem.* **1995**, *5*, 1953.
(59) He, Y.; Sahoo, Y.; Wang, S.; Luo, H.; Prasad, P. N.; Swihart, M. T. *J. Nanopart. Res.* **2006**, *8*, 335.
(60) Zhao, X. Q.; Zheng, F.; Liang, Y.; Hu, Z. Q.; Xu, Y. B. *Mater. Lett.* **1994**, *21*, 285.
(61) Veintemillas-Verdaguer, S.; Morales, M. P.; Serna, C. J. *Mater. Lett.* **1998**, *35*, 227.
(62) Alexandrescu, R.; Morjan, I.; Crunteanu, A.; Cojocaru, S.; Petcu, S.; Teodorescu, V.; Huisken, F.; Kohn, B.; Ehbrecht, M. *Mater. Chem. Phys.* **1998**, *55*, 115.
(63) Martelli, S.; Bomatí-Miguel, O.; de Dominics, L.; Giorgi, R.; Rinaldi, F.; Veintemillas-Verdaguer, S. *Appl. Surf. Sci.* **2002**, *186*, 562.
(64) Li, X. G.; He, Y. Q.; Talukdar, S. S.; Swihart, M. T. *Langmuir* **2003**, *19*, 8490.
(65) Belin, S.; Santos, L. R. B.; Briois, V.; Lusvardi, A.; Santilli, C. V.; Pulcinelli, S. H.; Chartier, T.; Larbot, A. *Colloids Surf., A* **2003**, *216*, 195.
(66) Cannas, C.; Casu, M.; Lai, A.; Musinu, A.; Piccaluga, G. *Phys. Chem. Chem. Phys.* **2002**, *4*, 2286.
(67) Casu, M.; Lai, A.; Musinu, A.; Piccaluga, G.; Solinas, S.; Bruni, S.; Cariati, F.; Beretta, E. *J. Mater. Sci.* **2001**, *36*, 3731.
(68) Cannas, C.; Casu, M.; Lai, A.; Musinu, A.; Piccaluga, G. *J. Mater. Chem.* **1999**, *9*, 1765.
(69) Prozorov, T.; Gedanken, A. *Adv. Mater.* **1998**, *10*, 532.
(70) Shafi, K. V. P. M.; Ulman, A.; Yan, X.; Yang, N.-L.; Estournes, C.; White, H.; Rafailovich, M. *Langmuir* **2001**, *17*, 5093.
(71) Li, G.; Chiba, A.; Takahashi, S.; Sato, M. *J. Appl. Phys.* **1997**, *83*, 3871.
(72) Atarashi, T.; Kim, Y. S.; Fujita, T.; Nakatsuka, K. *J. Magn. Magn. Mater.* **1999**, *201*, 7.
(73) Zboril, R.; Machala, L.; Mashlan, M.; Tucek, J.; Muller, R.; Schneeweiss, O. *Phys. Status Solidi C* **2004**, *1*, 3710.
(74) Xu, X. N.; Wolfus, Y.; Shaulov, A.; Yeshurun, Y. *J. Appl. Phys.* **2002**, *91*, 4611.
(75) Tronc, E.; Jolivet, J. P.; Livage, J. *Hyperfine Interact.* **1990**, *54*, 737.
(76) Barcova, K.; Mashlan, M.; Martinec, P. *Hyperfine Interact.* **2002**, *139/140*, 463.
(77) Dormann, J. L.; Fiorani, D.; Tronc, E. *J. Magn. Magn. Mater.* **1999,** *202*, 251.
(78) Casas, Ll.; Roig, A.; Molins, E.; Greneche, J.-M.; Asenjo, J.; Tejada, J. *Appl. Phys. A* **2002**, *74*, 591.
(79) Coey, J. M. D.; Readman, P. W. *Nature* **1973**, *246*, 476.
(80) Ferey, G.; Variet, F.; Coey J. M. D. *J. Phys.: Condens. Matter* **1979**, *12*, L531.
(81) Murad, E.; Johnston, H. *Mössbauer Spectroscopy Applied to Inorganic Chemistry*; Long, G., Ed.; Plenum: New York, 1987; Vol. 2, p 507.
(82) Guerault, H.; Tamine, M.; Greneche, *J.-M. J. Phys.: Condens. Matter* **2000**, *12*, 9497.
(83) Prozorov, R.; Yeshurun, Y.; Prozorov, T.; Gedanken, A. *Phys. Rev. B* **1999**, *59*, 6956.
(84) Martinez, B.; Roig, A.; Obradors, X.; Molins, E. *J. Appl. Phys.* **1996**, *79*, 2580.
(85) Pascal, C.; Pascal, J. L.; Favier, F. *Chem. Mater.* **1999**, *11*, 141.
(86) Zysler, R. D.; Fiorani, D.; Testa, A. M. *J. Magn. Magn. Mater.* **2001,** *224*, 5.
(87) Tartaj, P.; Serna, C. J. *Chem. Mater.* **2002**, *14*, 4396.
(88) Mørup, S.; Bødker, F.; Hendriksen, P. V.; Linderoth, S. *Phys. Rev. B* **1995**, *52*, 287.
(89) Fiorani, D.; Testa, A. M.; Lucari, F.; D'Orazio, F.; Romero, H. *Physica B* **2002**, *320*, 122.
(90) Batlle, X.; Labarta, A. *J. Phys. D: Appl. Phys.* **2002**, *35*, R15.
(91) Sohn, B. H.; Cohen, R. E.; Papaefthymiou, G. C. *J. Magn. Magn. Mater.* **1998,** *182*, 216.
(92) Leslie-Pelecky, D. L.; Rieke, R. D. *Chem. Mater.* **1996**, *8*, 1770.
(93) Shafi, K. V. P. M.; Koltypin, Y.; Gedanken, A. *J. Phys. Chem. B* **1997**, *101*, 6409.
(94) Morales, M. P.; Veintemillas-Verdaguer, S.; Montero, M. I.; Serna, C. J.; Roig, A.; Casas, L.; Martinez, B.; Sandiumenge, F. *Chem. Mater.* **1999**, *11*, 3058.
(95) Lin, S. Y.; Ferg, J.; Biswas, P.; Enzweiler, R.; Boolchand, P. *J. Magn. Magn. Mater.* **1996**, *159*, 147.
(96) Kodama, R. H.; Berkowitz, A. E. *Phys. Rev. B* **1999**, *59*, 6321.
(97) Jiang, J. Z.; Goya, G. F.; Rechenberg, H. R. *J. Phys.: Condens. Matter.* **1999**, *11*, 4063.
(98) Iglesias, O.; Labarta, A. *Phys. Rev. B* **2001**, *63*, 184416.
(99) Schneeweiss, O.; Zboril, R.; Pizurova, N.; Mashlan, M.; Petrovsky, E.; Tucek, J. *Nanotechnology* **2006**, *17*, 607.
(100) Dormann, J. L.; Fiorani, D.; Cherkaoui, R.; Tronc, E.; Lucari, F.; D'Orazio, F.; Spinu, L.; Nogues, M.; Kachkachi, H.; Jolivet, J.-P. *J. Magn. Magn. Mater.* **1999**, *203*, 23.
(101) Frandsen, C.; Ostenfeld, C. W.; Xu, M.; Jacobsen, C. S.; Keller, L.; Lefmann, K.; Mørup, S. *Phys. Rev. B* **2004**, *70*, 134416.
(102) Dutta, P.; Manivannan, A.; Seehra, M. S.; Shan, N.; Huffman, G. P. *Phys. Rev. B* **2004**, *70*, 174428.
(103) Dutta, P.; Manivannan, A.; Seehra, M. S.; Shan, N.; Huffman, G. P. *J. Appl. Phys.* **2006**, *99*, 08H105.
(104) Brice-Profeta, S.; Arrio, M.-A.; Tronc, E.; Menguy, N.; Letard, I.; Cartier dit Moulin, C.; Nogues, M.; Chaneac, C.; Jolivet, J.-P.; Sainctavit, Ph. *J. Magn. Magn. Mater.* **2005**, *288*, 354.
(105) Lai, J.; Shafi, K. V. P. M.; Loos, K.; Ulman, A.; Lee, Y.; Vogt, T.; Estournes, C. *J. Am. Chem. Soc.* **2003**, *125*, 11470.
(106) Jeong, J.-R.; Lee, S.-J.; Kim, J.-D.; Shin, S.-Ch. *Phys. Status Solidi B* **2004**, *241*, 1593.
(107) Mukadam, M. D.; Yusuf, S. M.; Sharma, P.; Kulshreshtha, S. K. *J. Magn. Magn. Mater.* **2004**, *272−274*, 1401.
(108) Tronc, E.; Ezzir, A.; Cherkaoui, R.; Chaneac, C.; Nogues, M.; Kachkachi, H.; Fiorani, D.; Tesla, A. M.; Greneche, J.-M.; Jolivet, J.-P. *J. Magn. Magn. Mater.* **2000**, *221*, 63.
(109) Fiorani, D.; Tesla, A. M; Suber, L.; Angiolini, M.; Montone, A.; Polichetti, M. *Nanostruct. Mater.* **1999**, *12*, 939.
(110) Bødker, F.; Hansen, M. F.; Koch, C. B.; Mørup, S. *Phys. Rev. B* **2000**, *61*, 6826.

(111) Zysler, R. D.; Vasquez-Mansilla, M.; Acriprete, C.; Dimitrijewits, M.; Rodriguez-Sierra, D.; Saragovi, C. *J. Magn. Magn. Mater.* **2001**, *224*, 39.

(112) De Grave, E.;Vochten, R.; Quenard, O.; Van San, E.; Desseyn, H.; Rousset, A. *Nanostruct. Mater.* **1999**, *11*, 493.

(113) Rojas, T. C.; Sanchez-Lopez, J. C.; Greneche, J.-M.; Conde, A.; Fernandez, A. *J. Mater. Sci.* **2004**, *39*, 4877.

(114) Kang, Y. S.; Lee, D. K.; Lee, Ch. S.; Stroeve, P. *J. Phys. Chem. B* **2002**, *106*, 9341.

(115) Hendriksen, P. V.; Oxborrow, C. A.; Linderoth, S.; Mørup, S.; Hanson, M.; Johansson, C.; Bødker, F.; Davies, K.; Charles, S. W.; Wells, S. *Nucl. Instrum. Methods Phys. Res., Sect. B* **1993**, *76*, 138.

(116) Da Costa, G. M.; De Grave, E.; Bowen, L. H.; Vandenberghe, R. E.; De Bakker, P. M. A. *Clays Clay Miner.* **1994**, *42*, 628.

(117) Johnson, C. E. *J. Phys. D: Appl. Phys.* **1996**, *29*, 2266.

(118) Pankhurst, Q. A.; Pollard, R. J. *J. Phys.: Condens. Matter* **1990**, *2*, 7329.

(119) Pankhurst, Q. A. *Hyperfine Interact.* **1994**, *90*, 201.